

# Polarization transfer measurements for $^{12}\text{C}(\vec{p}, \vec{n})^{12}\text{N}(\text{g.s.}, 1^+)$ at 296 MeV and nuclear correlation effects

M. Dozono,<sup>1,\*</sup> T. Wakasa,<sup>1</sup> E. Ihara,<sup>1</sup> S. Asaji,<sup>1</sup> K. Fujita,<sup>1</sup> K. Hatanaka,<sup>2</sup>  
M. Ichimura,<sup>3</sup> T. Ishida,<sup>4</sup> T. Kaneda,<sup>2</sup> H. Matsubara,<sup>2</sup> Y. Nagasue,<sup>1</sup> T. Noro,<sup>1</sup>  
Y. Sakemi,<sup>4</sup> Y. Shimizu,<sup>5</sup> H. Takeda,<sup>1</sup> Y. Tameshige,<sup>2</sup> A. Tamii,<sup>2</sup> and Y. Yamada<sup>1</sup>

<sup>1</sup>*Department of Physics, Kyushu University, Higashi, Fukuoka 812-8581, Japan*

<sup>2</sup>*Research Center for Nuclear Physics,*

*Osaka University, Ibaraki, Osaka 567-0047, Japan*

<sup>3</sup>*Faculty of Computer and Information Sciences,*

*Hosei University, Koganei, Tokyo 184-8584, Japan*

<sup>4</sup>*Cyclotron and Radioisotope Center,*

*Tohoku University, Aoba, Miyagi 980-8578, Japan*

<sup>5</sup>*Center for Nuclear Study, The University of Tokyo, Bunkyo, Tokyo 113-0033, Japan*

(Dated: November 18, 2018)

## Abstract

Differential cross sections and complete sets of polarization observables are presented for the Gamow-Teller  $^{12}\text{C}(\vec{p}, \vec{n})^{12}\text{N}(\text{g.s.}, 1^+)$  reaction at a bombarding energy of 296 MeV with momentum transfers  $q$  of 0.1 to 2.2  $\text{fm}^{-1}$ . The polarization transfer observables are used to deduce the spin-longitudinal cross section,  $ID_q$ , and spin-transverse cross sections,  $ID_p$  and  $ID_n$ . The data are compared with calculations based on the distorted wave impulse approximation (DWIA) using shell-model wave functions. Significant differences between the experimental and theoretical results are observed for all three spin-dependent  $ID_i$  at momentum transfers of  $q \gtrsim 0.5 \text{ fm}^{-1}$ , suggesting the existence of nuclear correlations beyond the shell model. We also performed DWIA calculations employing random phase approximation (RPA) response functions and found that the observed discrepancy is partly resolved by the pionic and rho-mesonic correlation effects.

PACS numbers: 24.70.+s, 25.40.Kv, 27.20.+n

---

\*Electronic address: dozono@phys.kyushu-u.ac.jp

## I. INTRODUCTION

Nuclear spin-isospin correlations produce various interesting phenomena in nuclei depending on the momentum transfer  $q$  [1]. At small momentum transfers,  $q \simeq 0 \text{ fm}^{-1}$ , the spin-isospin particle-hole interaction is strongly repulsive, which leads to such collective excitations in nuclei as the Gamow-Teller (GT) giant resonance. The quenching of the total strength of the GT transitions from its sum rule value has prompted theoretical studies of possible mechanisms, ranging from conventional configuration mixing to admixture of the  $\Delta$ -hole ( $\Delta$ -h) states. Recent experimental studies of  $^{90}\text{Zr}(p, n)$  and  $(n, p)$  reactions [2, 3] have revealed that the coupling to 2-particle-2-hole (2p-2h) excitations is the major source of quenching of the GT strengths, while  $\Delta$ -h coupling plays a minor role.

At fairly large momentum transfers,  $q \gtrsim 1 \text{ fm}^{-1}$ , the spin-transverse interaction induced by one rho-meson exchange remains repulsive, while the spin-longitudinal interaction driven by one pion exchange becomes attractive. This attraction of the spin-longitudinal interaction produces pion condensation and its precursor phenomena. Pion condensation [4] is expected to occur in neutron stars (NSs) such as 3C58 [5] and accelerate their cooling [6]. It is predicted that pion condensation does not occur in normal nuclei. However, precursor phenomena may be observed in normal nuclei if they are near the critical point of the phase transition. As possible evidence of a precursor, enhancements of the M1 cross section in proton inelastic scattering [7, 8] and of the ratio  $R_L/R_T$ , the spin-longitudinal (pionic) response function  $R_L$  to the spin-transverse (rho-mesonic) response function  $R_T$ , in the quasielastic scattering (QES) region [9, 10] were proposed at a momentum transfer of about  $q \simeq 1.7 \text{ fm}^{-1}$ . Motivated by these predictions, many experiments involving the M1 transition and QES have been carried out. These include the measurement of the  $^{12}\text{C}(p, p')^{12}\text{C}^*(1^+, T = 1)$  scattering at incident energies of about 120 to 800 MeV [11, 12, 13, 14], and the experimental extraction of  $R_L/R_T$  using complete sets of polarization transfer observables in  $(\vec{p}, \vec{p}')$  scattering [15, 16, 17, 18, 19] and  $(\vec{p}, \vec{n})$  reactions [20, 21, 22, 23, 24] on various targets at intermediate energies. However, these experimental data did not show the theoretically expected enhancements. Recent analysis of QES data shows pionic enhancement in the spin-longitudinal cross section representing  $R_L$ , which suggests that the lack of enhancement in the value of  $R_L/R_T$  is due to the rho-mesonic component [25]. The measurement of the pure pionic excitation of  $^{16}\text{O}(p, p')^{16}\text{O}^*(0^-, T = 1)$  scattering at  $T_p = 295 \text{ MeV}$  also supports such

an enhancement [26].

The analyses of QES and pure pionic excitation data suggest that one needs to reconsider the interpretation of the M1 data. The pionic effect in the M1 cross section might be masked by the contribution from the rho-mesonic component because the M1 state is a mixture of spin-longitudinal and spin-transverse states. In addition, proton inelastic scattering, including the M1 transition, mix isoscalar and isovector contributions. With respect to this issue, the GT  $^{12}\text{C}(p, n)^{12}\text{N}(\text{g.s.}, 1^+)$  reaction, which is the isobaric analog of the M1  $^{12}\text{C}(p, p')^{12}\text{C}^*(1^+, T = 1)$  scattering, has an advantage because the  $(p, n)$  reaction exclusively depends on the isovector contribution. Thus, it is interesting to study nuclear correlation effects in this reaction by separating the cross section into pionic and rho-mesonic components, using a complete set of polarization observables. However, no complete polarization transfer measurements for the GT reaction have been reported until now.

In this paper, we present differential cross sections and complete sets of polarization observables for the  $^{12}\text{C}(\vec{p}, \vec{n})^{12}\text{N}(\text{g.s.}, 1^+)$  reaction measured at  $T_p = 296$  MeV over a range of  $q = 0.1$  to  $2.2$  fm $^{-1}$ . This incident energy is ideal for studying GT transitions because the spin excitations are dominant in the  $(p, n)$  reaction near 300 MeV [27]. In addition, distortion effects are minimal around 300 MeV [1], thereby enabling one to extract reliable nuclear structure information such as nuclear correlation effects.

The differential cross section and a complete set of polarization transfer observables are used to separate the cross section into nonspin ( $ID_0$ ), spin-longitudinal ( $ID_q$ ), and two spin-transverse ( $ID_p$  and  $ID_n$ ) polarized cross sections. The spin-dependent polarized cross sections,  $ID_q$ ,  $ID_p$ , and  $ID_n$ , are compared with distorted wave impulse approximation (DWIA) calculations using random phase approximation (RPA) response functions, in order to assess the nuclear correlation effects quantitatively. The theoretical calculations give good descriptions of all of the spin-dependent polarized cross sections. These results demonstrate the existence of pionic and rho-mesonic correlations inside nuclei.

## II. EXPERIMENTAL METHODS

The experiment was performed using the Neutron Time-Of-Flight (NTOF) facility [28] and the neutron detector/polarimeter NPOL3 [29] at the Research Center for Nuclear Physics (RCNP) at Osaka University. Detailed descriptions of the NTOF facility and the

NPOL3 system can be found in Refs. [28, 29, 30, 31, 32, 33, 34, 35]. Only the details relevant to the present experiment are described here. Schematic layouts of the NTOF facility and the NPOL3 system are presented in Figs. 1 and 2, respectively. In Fig. 1, the coordinate systems for incident protons and outgoing neutrons are also shown.

### A. Polarized proton beam

The high intensity polarized ion source (HIPIS) [36] at RCNP was used to provide the proton beam. The direction of the beam polarization was reversed every 5 s in order to minimize geometrical false asymmetries that might be present in the experimental apparatus. The polarized proton beam from HIPIS was accelerated up to  $T_p = 53$  and 296 MeV by the Azimuthally Varying Field (AVF) [37] and Ring [38] cyclotrons, respectively. The radio frequency (rf) of the AVF cyclotron was 15.42 MHz, corresponding to a beam pulse period of 64.86 ns. In the cross section and analyzing power measurement, one out of every five beam pulses was selected prior to injection into the Ring cyclotron, yielding a pulse period of 324.3 ns. This pulse selection reduced the wrap-around events of slow neutrons from preceding beam pulses. In the measurement of the polarization transfer observables, the pulse selection was not performed, so as to achieve reasonable statistical accuracy. Note that the contribution from the wrap-around events was negligibly small ( $\lesssim 1\%$ ) because of the kinematical selection at the NPOL3 system (see Sec. III C). The single-turn extraction was maintained during these measurements in order to preserve the beam polarization.

Two superconducting solenoid magnets (SOL1 and SOL2) located in the injection line from the AVF to Ring cyclotrons were used to precess the proton spin. Each magnet can rotate the direction of the polarization vector from the normal  $\hat{N}$  into the sideways  $\hat{S}$  directions. These two magnets are separated by a bending angle of  $45^\circ$ , and thus the spin precession angle in this bending magnet is about  $85.2^\circ$  for  $T_p = 53$  MeV protons. Therefore, proton beams are obtained with longitudinal ( $\hat{L}$ ) and sideways ( $\hat{S}$ ) polarizations at the exit of SOL2 by using the SOL1 and SOL2 magnets, respectively.

The beam polarization was continuously monitored by two sets of beam line polarimeters (BLP1 and BLP2) [28, 30] after the Ring cyclotron. Each polarimeter consists of four conjugate-angle pairs of plastic scintillation detectors and determines the beam polarization via  ${}^1\text{H}(\vec{p}, p){}^1\text{H}$  scattering in the normal ( $\hat{N}$ ) and sideways ( $\hat{S}$ ) directions. A self-supporting

CH<sub>2</sub> target with a thickness of 1.1 mg/cm<sup>2</sup> was used as the hydrogen target, and the elastically scattered and recoil protons were detected in coincidence with a conjugate-angle pair of plastic scintillators. BLP1 and BLP2 are separated by a bending angle of 98°, and thus the spin precession angle in the bending magnet is about 231.1° for  $T_p = 296$  MeV protons. Therefore, all components ( $p_S, p_N, p_L$ ) of the beam polarization can be simultaneously determined using BLP1 and BLP2. The typical magnitude of the beam polarization was about 0.70.

### B. Target and NTOF facility

The NTOF facility [28], as illustrated in Fig. 1, consists of a beam swinger magnet, a neutron spin rotation (NSR) magnet, and a 100 m Time-Of-Flight (TOF) tunnel. The proton beam bombarded a self-supporting <sup>nat</sup>C (98.9% <sup>12</sup>C) target with a thickness of 89 mg/cm<sup>2</sup> in the beam swinger magnet. The target energy loss was estimated to be about 270 keV by using the stopping power of carbon for 296 MeV protons. Neutrons from the target entered the TOF tunnel and were detected using NPOL3 at the end of its flight path. Protons downstream of the target were swept up by the beam swinger magnet and stopped by a graphite beam stop (Faraday cup) from which the integrated beam current was measured. Typical beam currents were 50 and 500 nA for the cross section and polarization transfer measurements, respectively. The reaction angle was changed by repositioning the target along the beam trajectory inside the beam swinger magnet.

The NSR magnet was positioned at the entrance of the TOF tunnel. This magnet was used to precess the neutron polarization from the longitudinal  $\hat{L}'$  to the normal  $\hat{N}'$  directions, enabling the measurement of the longitudinal component of the neutron polarization with NPOL3 as the normal component. This magnet was also used for the measurement of the induced polarization  $P$  [23]. In this case, the neutron polarization was precessed in the  $N' - L'$  plane by about 120°, depending on the neutron kinetic energy.

### C. Neutron detector/polarimeter NPOL3

The NPOL3 system [29], illustrated in Fig. 2, consists of three planes of scintillation detectors. Each of the first two planes (HD1 and HD2) consists of 10 sets of one-dimensional

position-sensitive plastic scintillation counters (hodoscopes) with a size of  $100 \times 10 \times 5 \text{ cm}^3$ , covering an area of  $100 \times 100 \text{ cm}^2$ . The last plane (NC) is a two-dimensional position-sensitive liquid scintillation counter with a size of  $100 \times 100 \times 10 \text{ cm}^3$ . Both HD1 and HD2 served as neutron detectors and neutron polarization analyzers for the cross section and polarization transfer measurements, respectively, and NC acted as a catcher for the particles scattered by HD1 or HD2 in the polarization transfer measurements. Thin plastic scintillator planes (CPV and CPD) in front of HD1 and NC were used to veto and identify charged particles, respectively.

The neutron energy was determined by the TOF to a given hodoscope with respect to the rf signal of the AVF cyclotron. A peak from  $^{12}\text{C}(p, n)^{12}\text{N}(\text{g.s.})$  provided a time reference for the absolute timing calibration. The overall energy resolution in full width at half maximum (FWHM) was about 500 keV, mainly due to the target energy loss and the beam pulse width with contributions of about 270 and 350 keV, respectively.

### III. DATA REDUCTION

#### A. Polarization observables

A complete set of polarization observables,  $A_y$ ,  $P$ , and  $D_{ij}(i = S', N', L'; j = S, N, L)$ , for a parity conserving reaction relates the outgoing neutron polarization  $\mathbf{p}' = (p'_{S'}, p'_{N'}, p'_{L'})$  to the incident proton polarization  $\mathbf{p} = (p_S, p_N, p_L)$  according to

$$\begin{pmatrix} p'_{S'} \\ p'_{N'} \\ p'_{L'} \end{pmatrix} = \left[ \begin{pmatrix} D_{S'S} & 0 & D_{S'L} \\ 0 & D_{NN} & 0 \\ D_{L'S} & 0 & D_{L'L} \end{pmatrix} \begin{pmatrix} p_S \\ p_N \\ p_L \end{pmatrix} + \begin{pmatrix} 0 \\ P \\ 0 \end{pmatrix} \right] \frac{1}{1 + p_N A_y}. \quad (1)$$

The directions of the coordinate system (sideways  $S$ , normal  $N$ , and longitudinal  $L$ ) are defined in terms of the incident proton momentum  $\mathbf{k}_{\text{lab}}$  and the outgoing neutron momentum  $\mathbf{k}'_{\text{lab}}$  in the laboratory frame as  $\hat{\mathbf{L}} = \hat{\mathbf{k}}_{\text{lab}}$ ,  $\hat{\mathbf{L}}' = \hat{\mathbf{k}}'_{\text{lab}}$ ,  $\hat{\mathbf{N}} = \hat{\mathbf{N}}' = (\hat{\mathbf{k}}_{\text{lab}} \times \hat{\mathbf{k}}'_{\text{lab}}) / |\hat{\mathbf{k}}_{\text{lab}} \times \hat{\mathbf{k}}'_{\text{lab}}|$ ,  $\hat{\mathbf{S}} = \hat{\mathbf{N}} \times \hat{\mathbf{L}}$ , and  $\hat{\mathbf{S}}' = \hat{\mathbf{N}}' \times \hat{\mathbf{L}}'$ .

The analyzing power  $A_y$ , the induced polarization  $P$ , and the polarization transfer observable  $D_{NN}$  were measured for a normally ( $\hat{N}$ ) polarized proton beam. The other polarization transfer observables,  $D_{S'S}$ ,  $D_{L'S}$ ,  $D_{S'L}$ , and  $D_{L'L}$ , were obtained from measurements with two kinds of proton beams polarized in the horizontal plane. Note that the polarization axes of these beams were almost orthogonal to each other. Therefore, the efficiency of measuring  $D_{ij}$  is almost the same as that for pure sideways ( $\hat{S}$ ) and longitudinal ( $\hat{L}$ ) polarized proton beams [23].

### B. Neutron detection efficiency

The differential cross section  $(d\sigma/d\Omega)_{\text{lab}}$  in the laboratory frame is related to the observed neutron yield  $N_n$  as

$$\left(\frac{d\sigma}{d\Omega}\right)_{\text{lab}} = \frac{N_n}{N_p \rho \Delta\Omega \varepsilon T f_{\text{live}}}, \quad (2)$$

where  $N_p$  is the number of incident protons,  $\rho$  is the target density,  $\Delta\Omega$  and  $\varepsilon$  are the solid angle and intrinsic neutron detection efficiency of NPOL3 (HD1 and HD2), respectively,  $T$  is the neutron transmission factor along the flight path in the air, and  $f_{\text{live}}$  is the live time ratio.

The product  $\varepsilon T$  was determined by measuring the neutron yield from the  $0^\circ$   ${}^7\text{Li}(p, n){}^7\text{Be}(\text{g.s.} + 0.43 \text{ MeV})$  reaction which has a constant center of mass (c.m.) cross section of  $(d\sigma/d\Omega)_{\text{c.m.}} = 27.0 \pm 0.8 \text{ mb/sr}$  at an incident energy range of  $T_p = 80\text{--}795 \text{ MeV}$  [39]. A self-supporting  ${}^7\text{Li}$  (99.97%) target with a thickness of  $54 \text{ mg/cm}^2$  was used. The  $\varepsilon T$  value was  $0.051 \pm 0.003$  where the uncertainty comes mainly from the uncertainties in the cross section for the  $0^\circ$   ${}^7\text{Li}(p, n){}^7\text{Be}(\text{g.s.} + 0.43 \text{ MeV})$  reaction (3%) and in the thickness of the  ${}^7\text{Li}$  target (3%). We note that the transmission factor  $T$  has been assumed to be independent of reaction angle because the dependence of the flight length on reaction angle is very small ( $\lesssim 1\%$ ).

### C. Effective analyzing power

The neutron polarization was analyzed using  $\vec{n} + p$  and quasi-elastic  $\vec{n} + \text{C}$  scattering in analyzer HD1 or HD2, and the recoiled protons were detected with catcher NC. These events were kinematically resolved from background events such as wrap-around and the

target gamma rays by using time and position information from the analyzer and catcher planes. Both the normal  $N'$  and sideways  $S'$  components of the neutron polarization were measured simultaneously, with an azimuthal distribution of  $\vec{n} + p$  and quasi-elastic  $\vec{n} + C$  events.

The effective analyzing power  $A_{y;\text{eff}}$  of NPOL3 was measured using polarized neutrons from the GT  $^{12}\text{C}(\vec{p}, \vec{n})^{12}\text{N}(\text{g.s.})$  reaction at  $\theta_{\text{lab}} = 0^\circ$ . Two kinds of polarized protons having normal ( $p_N$ ) and longitudinal ( $p_L$ ) polarizations were used. The corresponding neutron polarizations are  $p'_N = p_N D_{NN}(0^\circ)$  and  $p'_L = p_L D_{LL}(0^\circ)$  where  $D_{NN}(0^\circ)$  and  $D_{LL}(0^\circ)$  represent the polarization transfer observables at  $\theta_{\text{lab}} = 0^\circ$ . Then the asymmetries,  $\epsilon_N$  and  $\epsilon_L$ , measured by NPOL3 are

$$\begin{aligned}\epsilon_N &= p'_N A_{y;\text{eff}} = p_N D_{NN}(0^\circ) A_{y;\text{eff}}, \\ \epsilon_L &= p'_L A_{y;\text{eff}} = p_L D_{LL}(0^\circ) A_{y;\text{eff}}.\end{aligned}\tag{3}$$

As described in Sec II B, the asymmetry  $\epsilon_L$  was measured as the normal component using the NSR magnet. Because the polarization transfer observables  $D_{ii}(0^\circ)$  for the GT transition satisfy [40]

$$2D_{NN}(0^\circ) + D_{LL}(0^\circ) = -1,\tag{4}$$

$A_{y;\text{eff}}$  can be expressed as

$$A_{y;\text{eff}} = - \left( 2 \frac{\epsilon_N}{p_N} + \frac{\epsilon_L}{p_L} \right)\tag{5}$$

using Eqs. (3) and (4). Thus, one obtains the  $A_{y;\text{eff}}$  value without knowing ahead of time the  $D_{ii}(0^\circ)$  values. The resulting  $A_{y;\text{eff}}$  is  $0.191 \pm 0.016$  where the uncertainty includes the statistical ( $\simeq 6\%$ ) and systematic ( $\simeq 2\%$ ) uncertainties. The systematic uncertainty is estimated by considering the uncertainty of the beam polarization [30].

#### D. Peak fitting

Figure 3 shows typical excitation energy spectra of  $^{12}\text{C}(p, n)^{12}\text{N}$  at four momentum transfers of  $q = 0.14, 0.7, 1.2,$  and  $1.7 \text{ fm}^{-1}$ . The GT  $1^+$  state at  $E_x = 0 \text{ MeV}$  (ground state of  $^{12}\text{N}$ ) gives rise to a prominent peak at small momentum transfers. At large momentum transfers, on the other hand, its peak is small and not fully resolved from a large peak consisting of excited states with  $J^\pi = 2^+$  and  $2^-$  at  $E_x = 0.96$  and  $1.19 \text{ MeV}$ , respectively. Therefore, peak fitting was performed to extract the yield of the GT  $1^+$  state. The spectra



were fitted at  $E_x < 1.5$  MeV where the excited states at  $E_x = 0.96$  and 1.19 MeV were treated as a single peak because the present energy resolution could not resolve them. The continuum background from wrap-around and  $^{13}\text{C}(p, n)$  events was considered to be a linear function of  $E_x$ . The dashed curves in Fig. 3 show the fitting results for the individual peaks, while the solid curves show the sum of these contributions including the background indicated as the straight dotted lines. The peak fittings at all momentum transfers sufficed to extract the GT  $1^+$  yield.

## IV. RESULTS AND ANALYSIS

### A. Cross section and polarization observables

Figure 4 shows the cross section for the  $^{12}\text{C}(p, n)^{12}\text{N}(\text{g.s.}, 1^+)$  reaction at  $T_p = 296$  MeV as a function of the momentum transfer  $q$ . The corresponding reaction angle  $\theta_{\text{c.m.}}$  is also shown on the top of the figure. The momentum transfer resolution is about  $0.04 \text{ fm}^{-1}$  which is mainly due to the finite solid angle of the detector. As seen in Fig. 3, the GT state is not clearly resolved from the neighboring states, and thus there is a correlation between the yields of these two components in the peak fitting. By considering the uncertainties of the GT yields due to this correlation, we have estimated the systematic uncertainties. The shaded boxes show the uncertainties including statistical and systematic uncertainties. The statistical and systematic uncertainties at large momentum transfers of  $q \simeq 1.6 \text{ fm}^{-1}$  are about 2% and 4%, respectively. A 6% uncertainty due to the cross section normalization (see Sec. III B) is not included. The open circles and open triangles, respectively, are data for the same reaction [41] and the analogous  $^{12}\text{C}(p, p')^{12}\text{C}^*(1^+, T = 1)$  scattering [42] at  $T_p = 295$  MeV. The  $^{12}\text{C}(p, p')$  data have been multiplied by a factor of two because of the difference in the isospin Clebsch-Gordan (CG) coefficients between  $^{12}\text{C}(p, n)$  and  $^{12}\text{C}(p, p')$ . Our data are consistent with the previous data within the statistical and systematic uncertainties.

In Fig. 5, a complete set of polarization observables,  $D_{ij}$ ,  $A_y$ , and  $P$ , are presented for the  $^{12}\text{C}(\vec{p}, \vec{n})^{12}\text{N}(\text{g.s.}, 1^+)$  reaction at  $T_p = 296$  MeV as a function of momentum transfer. In the top right panel, the  $A_y$  and  $P$  data are shown as filled and open circles, respectively, and the  $P$  data are offset by a momentum transfer of  $0.05 \text{ fm}^{-1}$  for clarity. The error bars represent statistical uncertainties only, while the shaded and open boxes include the systematic uncer-

tainties. The statistical and systematic uncertainties in  $D_{ij}$  for large momentum transfers of  $q \gtrsim 1.0 \text{ fm}^{-1}$  are about 0.19–0.24 and 0.21–0.26, respectively, which are satisfactory for discussing nuclear correlation effects in this momentum transfer range.

## B. DWIA calculations with shell-model wave function

We performed microscopic DWIA calculations using the computer code DW81 [43], which treats the knock-on exchange amplitude exactly. Distorted waves were generated using a global optical model potential (OMP) optimized for  $^{12}\text{C}$  in the proton energy range of  $T_p = 20\text{--}1040 \text{ MeV}$  [44, 45], with the Coulomb term turned off for the exit channel. The nucleon-nucleon ( $NN$ )  $t$ -matrix parameterized by Franey and Love (FL) [27] at 325 MeV was used as the interaction between the incident and struck nucleons. The one-body density matrix elements (OBDMs) were obtained from shell-model calculations using the computer code OXBASH [46]. These calculations were performed in the  $0\hbar\omega$   $p$ -shell model space using the Cohen-Kurath wave functions (CKWFs) [47] based on the (6–16) 2BME interaction. The transition form factor was normalized to reproduce the observed beta-decay  $ft$  value of 13178 s [48] which corresponds to a GT strength  $B(\text{GT})$  of 0.873 [49]. The radial part of the single-particle wave functions was generated by a Woods-Saxon (WS) potential with  $r_0 = 1.27 \text{ fm}$ ,  $a_0 = 0.67 \text{ fm}$  [50], and a spin-orbit potential depth of  $V_{\text{so}} = 6.5 \text{ MeV}$  [51]. The depths of the WS potential were adjusted to reproduce the separation energies for the  $0p_{3/2}$  orbits.

The solid curves in Figs. 4 and 5 show the results of the calculations. The normalization factor for the transition form factor is  $N = 0.94$ . These calculations reproduce the experimental data reasonably well at small momentum transfers of  $q \lesssim 0.5 \text{ fm}^{-1}$  but show poor agreement with the data at  $q \gtrsim 0.5 \text{ fm}^{-1}$ . In particular, the calculations shift the momentum transfer dependence of the cross section to larger momentum transfers and underestimate the cross section at  $q \simeq 1.6 \text{ fm}^{-1}$ . In order to investigate the reason for this discrepancy, we next separated the cross section into polarized cross sections using the polarization observables.

### C. Polarized cross sections

The cross section  $I$  ( $(d\sigma/d\Omega)_{\text{c.m.}}$  in Fig. 4) can be separated into four polarized cross sections  $ID_i$  as

$$I = ID_0 + ID_q + ID_n + ID_p, \quad (6)$$

where  $D_i$  are the c.m. polarization observables introduced by Bleszynski *et al.* [52]. The c.m. coordinate system  $(q, n, p)$  is defined as  $\hat{\mathbf{q}} = (\mathbf{k}' - \mathbf{k})/(|\mathbf{k}' - \mathbf{k}|)$ ,  $\hat{\mathbf{n}} = (\mathbf{k} \times \mathbf{k}')/(|\mathbf{k} \times \mathbf{k}'|)$ , and  $\hat{\mathbf{p}} = \hat{\mathbf{q}} \times \hat{\mathbf{n}}$ , where  $\mathbf{k}$  and  $\mathbf{k}'$  are the momenta of the incident and outgoing nucleons in the c.m. frame, respectively. The  $D_i$  values are related to  $D_{ij}$  in the laboratory frame according to [53]

$$\begin{aligned} D_0 &= \frac{1}{4}[1 + D_{NN} + (D_{S'S} + D_{L'L}) \cos \alpha_1 \\ &\quad + (D_{L'S} - D_{S'L}) \sin \alpha_1], \\ D_n &= \frac{1}{4}[1 + D_{NN} - (D_{S'S} + D_{L'L}) \cos \alpha_1 \\ &\quad - (D_{L'S} - D_{S'L}) \sin \alpha_1], \\ D_q &= \frac{1}{4}[1 - D_{NN} + (D_{S'S} - D_{L'L}) \cos \alpha_2 \\ &\quad - (D_{L'S} + D_{S'L}) \sin \alpha_2], \\ D_p &= \frac{1}{4}[1 - D_{NN} - (D_{S'S} - D_{L'L}) \cos \alpha_2 \\ &\quad + (D_{L'S} + D_{S'L}) \sin \alpha_2], \end{aligned} \quad (7)$$

where  $\alpha_1 \equiv \theta_{\text{lab}} + \Omega$  and  $\alpha_2 \equiv 2\theta_p - \theta_{\text{lab}} - \Omega$ . Here  $\theta_p$  is the angle between  $\hat{\mathbf{k}}$  and  $\hat{\mathbf{p}}$ , and  $\Omega$  is the relativistic spin rotation angle defined in Ref. [53]. For a plane-wave impulse approximation with eikonal approximation, the polarized cross sections  $ID_i$  can be expressed as [53]

$$\begin{aligned} ID_0 &= 4KN_D (|A|^2 R_0 + |C|^2 R_n), \\ ID_n &= 4KN_D (|B|^2 R_n + |C|^2 R_0), \\ ID_q &= 4KN_D (|E|^2 R_q + |D|^2 R_p), \\ ID_p &= 4KN_D (|F|^2 R_p + |D|^2 R_q), \end{aligned} \quad (8)$$

where  $K$  is a kinematical factor,  $N_D$  is a distortion factor,  $A-F$  are the components of the  $NN$   $t$ -matrix, and  $R_i$  are the response functions. Figure 6 shows the squared  $t$ -matrix components corresponding to each  $ID_i$ . These components are derived from the FL  $t$ -matrix at 325 MeV. The effect of the relativistic spin rotation is so small that the  $D$  term can be neglected. Thus, polarized cross sections  $ID_q$  and  $ID_p$  represent spin-longitudinal ( $R_q$ ) and spin-transverse ( $R_p$ ) components exclusively. At forward angles, where the spin-orbit component  $|C|^2$  is very small, polarized cross sections  $ID_0$  and  $ID_n$  represent nonspin ( $R_0$ ) and spin-transverse ( $R_n$ ) components, respectively.

Figure 7 shows four polarized cross sections  $ID_i$  as a function of momentum transfer. The meaning of the error bars and shaded boxes is the same as those in Figs. 4 and 5. Although the present GT transition does not have a nonspin response function  $R_0$ , the nonspin polarized cross section  $ID_0$  has a nonzero value due to the spin-orbit component  $|C|^2$  in Eq. (8). Since  $ID_0$  is small, we will only discuss the spin-dependent polarized cross sections  $ID_q$ ,  $ID_p$ , and  $ID_n$ . The oscillatory pattern for the spin-longitudinal cross section  $ID_q$  is different from those for the spin-transverse cross sections,  $ID_p$  and  $ID_n$ . As seen in Fig. 6, these patterns reflect the momentum transfer dependences of the corresponding  $NN$   $t$ -matrix components. Compared with the spin-transverse  $t$ -matrix components  $|B|^2$  and  $|F|^2$ , the spin-longitudinal component  $|E|^2$  has the first minimum at lower momentum transfer of  $q \simeq 0.7 \text{ fm}^{-1}$ . This is because the real part of  $E$  crosses zero near this momentum transfer due to the smallness of the pion mass. Thus the corresponding spin-longitudinal  $ID_q$  shows the first minimum at  $q \simeq 0.6 \text{ fm}^{-1}$ . Therefore, the data verify suitable separation in the spin-longitudinal and spin-transverse modes based on the reaction mechanism of Ref. [53].

The solid curves in Fig. 7 present the DWIA results with a shell-model wave function where the input parameters are same as those described in Sec IV B. The calculations underestimate all three spin-dependent  $ID_i$  at  $q \simeq 1.6 \text{ fm}^{-1}$ , and the discrepancy in the momentum transfer dependence is evident in the spin-transverse  $ID_p$  and  $ID_n$ . Thus, in Fig. 8, the sensitivity of the DWIA calculations for three spin-dependent  $ID_i$  was investigated for changes in the parameters. Note that the solid curves are the same as those in Fig. 7. First, the OMP dependence of the calculations was examined by using other OMPs; three global OMPs (EDAD Fit 1–3) parameterized for  $^{12}\text{C}$ – $^{208}\text{Pb}$  in the proton energy range of  $T_p = 20$ – $1040$  MeV [44, 45] and the OMP obtained from proton elastic scattering data on  $^{12}\text{C}$  at  $T_p = 318$  MeV whose parameters are listed in Table I [54]. The radial dependences of

Potential	$V_i$ (MeV)	$r_i$ (fm)	$a_i$ (fm)
Real central ( $i = R$ )	-5.005	1.272	0.411
Imaginary central ( $i = I$ )	-22.55	1.083	0.474
Real spin-orbit ( $i = RSO$ )	-1.77	0.910	0.867
Imaginary spin-orbit ( $i = ISO$ )	2.71	0.909	0.467
Coulomb ( $i = C$ )		1.24	

TABLE I: The optical model parameters obtained from proton elastic scattering data on  $^{12}\text{C}$  at  $T_p = 318$  MeV [54]. The potential is defined by  $U(r) = V_C(r) + V_R f_R(r) + iV_I f_I(r) + [\hbar/(m_\pi c)]^2 (1/r) [V_{RSO}(d/dr) f_{RSO}(r) + iV_{ISO}(d/dr) f_{ISO}(r)] (\boldsymbol{\sigma} \times \mathbf{L})$ , where  $V_C$  is the coulomb potential for a uniformly charged sphere and  $f_i(r) = [1 + \exp\{(r - r_i A^{1/3})/a_i\}]^{-1}$ .

these OMPs for the incident channel are shown in Fig. 9, and the DWIA results are shown in Fig. 8(a) by the bands. The OMP dependence of the spin-longitudinal  $ID_q$  is small, whereas those of the spin-transverse  $ID_p$  and  $ID_n$  are significantly larger near the cross section minimum at  $q \simeq 1.4 \text{ fm}^{-1}$ . We also performed DWIA calculations using the neutron global OMPs for  $^{12}\text{C}$ – $^{238}\text{U}$  in the neutron energy range of  $T_n = 20$ – $1000$  MeV [55] for the exit channel, and the results are plotted as the dashed curves in Fig. 8(a). The use of the neutron global OMPs gives larger values near the cross section minimum at  $q \gtrsim 1.4 \text{ fm}^{-1}$  in the spin-transverse mode. However, neither the discrepancy in the angular distribution nor the underestimation in the cross section at large momentum transfers can be explained by the OMP uncertainties.

Second, the proton-particle and neutron-hole configuration dependences were investigated. The bands in Fig. 8(b) are DWIA results with other CKWFs based on the (8–16) 2BME and (8–16) POT interactions [47]. We also performed DWIA calculations for a pure  $0p_{1/2}0p_{3/2}^{-1}$  transition from the Hartree-Fock (HF) state of  $^{12}\text{C}$  (the state fully occupying the  $0s_{1/2}$  and  $0p_{3/2}$  orbits), and the results are shown as the dashed curves. Table II summarizes the OBDMEs and  $B(\text{GT})$  together with the corresponding normalization factors  $N$  for the transition form factors. The configuration dependence is small for all three  $ID_i$ , and thus the discrepancy between the experimental and theoretical results is not resolved by considering the configuration dependence.

shell-model wave function	OBDME				$B(\text{GT})$	$N$
	$0p_{1/2}0p_{1/2}^{-1}$	$0p_{1/2}0p_{3/2}^{-1}$	$0p_{3/2}0p_{1/2}^{-1}$	$0p_{3/2}0p_{3/2}^{-1}$		
(6-16)2BME	0.0859	0.6672	0.3228	0.0925	0.929	0.94
(8-16)2BME	0.0733	0.6915	0.3262	0.0822	0.992	0.88
(8-16)POT	0.0582	0.6902	0.3393	0.0763	0.921	0.95
Pure $0p_{1/2}0p_{3/2}^{-1}$	0.0	1.0	0.0	0.0	5.228	0.17

TABLE II: One-body density matrix elements and Gamow-Teller strengths for the  $^{12}\text{C}(p, n)^{12}\text{N}(\text{g.s.}, 1^+)$  reaction used in the DWIA calculations. The normalization factors for the transition form factors are also listed.

Finally, we investigated the dependence on the radial wave function. The dashed curves in Fig. 8(c) are DWIA results using a harmonic oscillator (HO) potential with a size parameter of  $b = 1.53 \text{ fm}^{-1}$ . This parameter was obtained from an analysis of the electron scattering on  $^{12}\text{C}$  to the stretched  $4^-$ ,  $T = 1$  state at  $E_x = 19.55 \text{ MeV}$  [56] with the center-of-mass correction taken into account [57]. The results are almost the same as those for the WS potential. Thus the discrepancy between the experimental and theoretical results could not be explained by the radial wave function dependence.

Figure 10 represents the parameter dependence for the orthogonal components of the polarization transfer observables,  $D_{NN}$  (left panels),  $D_{S'S}$  (middle panels), and  $D_{L'L}$  (right panels). Based on the calculations in Figs. 8 and 10, the experimental data at large momentum transfers cannot be reproduced within the framework of the DWIA employing shell-model wave functions. Therefore, in the following section, nuclear correlation effects beyond the shell model are investigated.

## V. DISCUSSION

In this section, the experimental spin-dependent polarized cross sections are compared with the DWIA calculations using RPA response functions in order to investigate the nuclear correlation effects beyond the shell model.

### A. DWIA+RPA calculations

We performed DWIA+RPA calculations using the computer code CRDW [58]. The formalism of the calculations is discussed in Refs. [51, 58]. The spin–isospin response functions were calculated in a continuum RPA including the  $\Delta$  degrees of freedom. We further utilized a ring approximation [58], and used the  $\pi + \rho + g'$  model interaction for the effective interaction, which is expressed as [1]

$$V_{\text{eff}}(\mathbf{q}, \omega) = V_L(\mathbf{q}, \omega) + V_T(\mathbf{q}, \omega), \quad (9)$$

where  $V_L$  and  $V_T$  are the spin-longitudinal and spin-transverse effective interactions, respectively. They are determined by the pion and rho-meson exchange interactions and the Landau-Migdal (LM) interaction specified by the LM parameters,  $g'_{NN}$ ,  $g'_{N\Delta}$ , and  $g'_{\Delta\Delta}$ , as

$$\begin{aligned} V_L(\mathbf{q}, \omega) = & \frac{f_{\pi NN}^2}{m_\pi^2} \left( g'_{NN} + \frac{q^2}{\omega^2 - q^2 - m_\pi^2} \Gamma_{\pi NN}^2(q, \omega) \right) (\boldsymbol{\sigma}_1 \cdot \hat{\mathbf{q}})(\boldsymbol{\sigma}_2 \cdot \hat{\mathbf{q}})(\boldsymbol{\tau}_1 \cdot \boldsymbol{\tau}_2) \\ & + \frac{f_{\pi NN} f_{\pi N\Delta}}{m_\pi^2} \left( g'_{N\Delta} + \frac{q^2}{\omega^2 - q^2 - m_\pi^2} \Gamma_{\pi NN}(q, \omega) \Gamma_{\pi N\Delta}(q, \omega) \right) \\ & \times [\{(\boldsymbol{\sigma}_1 \cdot \hat{\mathbf{q}})(\mathbf{S}_2 \cdot \hat{\mathbf{q}})(\boldsymbol{\tau}_1 \cdot \mathbf{T}_2) + (1 \leftrightarrow 2)\} + \text{h.c.}] \\ & + \frac{f_{\pi N\Delta}^2}{m_\pi^2} \left( g'_{\Delta\Delta} + \frac{q^2}{\omega^2 - q^2 - m_\pi^2} \Gamma_{\pi N\Delta}^2(q, \omega) \right) \\ & \times \left[ \left\{ (\mathbf{S}_1 \cdot \hat{\mathbf{q}})(\mathbf{S}_2^\dagger \cdot \hat{\mathbf{q}})(\mathbf{T}_1 \cdot \mathbf{T}_2^\dagger) + (\mathbf{S}_1 \cdot \hat{\mathbf{q}})(\mathbf{S}_2 \cdot \hat{\mathbf{q}})(\mathbf{T}_1 \cdot \mathbf{T}_2) \right\} + \text{h.c.} \right], \end{aligned} \quad (10)$$

and

$$\begin{aligned} V_T(\mathbf{q}, \omega) = & \frac{f_{\pi NN}^2}{m_\pi^2} \left( g'_{NN} + C_\rho \frac{q^2}{\omega^2 - q^2 - m_\rho^2} \Gamma_{\rho NN}^2(q, \omega) \right) \\ & \times (\boldsymbol{\sigma}_1 \times \hat{\mathbf{q}})(\boldsymbol{\sigma}_2 \times \hat{\mathbf{q}})(\boldsymbol{\tau}_1 \cdot \boldsymbol{\tau}_2) \\ & + \frac{f_{\pi NN} f_{\pi N\Delta}}{m_\pi^2} \left( g'_{N\Delta} + C_\rho \frac{q^2}{\omega^2 - q^2 - m_\rho^2} \Gamma_{\rho NN}(q, \omega) \Gamma_{\rho N\Delta}(q, \omega) \right) \\ & \times [\{(\boldsymbol{\sigma}_1 \times \hat{\mathbf{q}})(\mathbf{S}_2 \times \hat{\mathbf{q}})(\boldsymbol{\tau}_1 \cdot \mathbf{T}_2) + (1 \leftrightarrow 2)\} + \text{h.c.}] \\ & + \frac{f_{\pi N\Delta}^2}{m_\pi^2} \left( g'_{\Delta\Delta} + C_\rho \frac{q^2}{\omega^2 - q^2 - m_\rho^2} \Gamma_{\rho N\Delta}^2(q, \omega) \right) \\ & \times \left[ \left\{ (\mathbf{S}_1 \times \hat{\mathbf{q}})(\mathbf{S}_2^\dagger \times \hat{\mathbf{q}})(\mathbf{T}_1 \cdot \mathbf{T}_2^\dagger) + (\mathbf{S}_1 \times \hat{\mathbf{q}})(\mathbf{S}_2 \times \hat{\mathbf{q}})(\mathbf{T}_1 \cdot \mathbf{T}_2) \right\} + \text{h.c.} \right], \end{aligned} \quad (11)$$

where  $m_\pi$  and  $m_\rho$  are the pion and rho-meson masses,  $\sigma$  and  $\tau$  are the spin and isospin operators of the nucleon  $N$ , and  $\mathbf{S}$  and  $\mathbf{T}$  are the spin and isospin transition operators from  $N$  to  $\Delta$ . The coupling constants and meson parameters for the pion and rho-meson exchange interactions from a Bonn potential were used, which treats  $\Delta$  explicitly [59]. The LM interaction effectively represents the short range correlations and the exchange terms in the RPA, and the LM parameters have been estimated to be  $g'_{NN} = 0.65 \pm 0.15$  and  $g'_{N\Delta} = 0.35 \pm 0.15$  [60] by using the peak position of the GT giant resonance and the GT quenching factor at  $q = 0 \text{ fm}^{-1}$  [2, 3], as well as the isovector spin-longitudinal polarized cross section in the QES process at  $q \simeq 1.7 \text{ fm}^{-1}$  [25]. We fixed  $g'_{\Delta\Delta} = 0.5$  [61] because the  $g'_{\Delta\Delta}$  dependence in the results is weak. The response functions are normalized to reproduce the experimental  $B(\text{GT})$ .

The ground state of  $^{12}\text{C}$  was assumed to be a HF state. However, as seen in Table II, the ground state correlation which is included in the shell-model calculations plays an important role in reproducing the experimental  $B(\text{GT})$  value of 0.873. In order to include the shell-model (configuration-mixing) effects effectively, we used much smaller normalization factors  $N$  than those of the shell-model calculations, namely  $N = 0.28$  and  $N = 0.17$  in the calculations with and without RPA correlations, respectively.

The nonlocality of the nuclear mean field was treated using the local effective mass approximation [1] in the form

$$m^*(r) = m_N - \frac{f_{\text{WS}}(r)}{f_{\text{WS}}(0)}(m_N - m^*(0)), \quad (12)$$

where  $m_N$  is the nucleon mass and  $f_{\text{WS}}(r)$  is a WS radial form. Here we adapted the standard value of  $m^*(0) = 0.7m_N$  [62, 63].

We used the same OMPs and single-particle wave functions as described in Sec. IV B. The  $NN$   $t$ -matrix parameterized by Franey and Love at 325 MeV was used, and the exchange terms were approximated by contact terms following the prescription by Love and Franey [64].

In Fig. 11, the consistency between theoretical results using the computer codes CRDW and DW81 is checked. The solid curves are the CRDW results with a free response function employing  $m^*(0) = m_N$ , whereas the dashed curves are the DW81 results with the corresponding wave function as for the dashed curves in Fig. 8(b). The normalization factor  $N$  of 0.17 is common, and both calculations for the unpolarized cross section  $I$  are in good



agreement with each other. The theoretical results for  $ID_i$  show good consistency except near the cross section minimum at  $q \simeq 1.4 \text{ fm}^{-1}$ . Therefore, in the next subsection, the experimental data are compared with the DWIA calculations using CRDW in order to investigate nuclear structure effects which could not be included in the preceding calculations, such as RPA correlations.

### B. Comparison with DWIA+RPA calculations

First, the nonlocality of the nuclear mean field was investigated. The dotted and dashed curves in Fig. 12 show the DWIA results with a free response function using  $m^*(0) = m_N$  and  $m^*(0) = 0.7m_N$ , respectively, and  $N = 0.17$ . The angular distributions of all three spin-dependent  $ID_i$  curves shift to lower momentum transfer due to the nonlocality of the nuclear mean field, so that the agreement with the data is improved. This shift arises because the transition form factor moves outward due to the Perey effect [65]. However, there remains a discrepancy between the experimental and theoretical results at around  $q \simeq 1.6 \text{ fm}^{-1}$ .

Next we considered the nuclear correlation effects in the RPA. The solid curves in Fig. 12 show the results of DWIA+RPA calculations using  $g'_{NN} = 0.65$ ,  $g'_{N\Delta} = 0.35$ , and  $m^*(0) = 0.7m_N$  with  $N = 0.28$ . The bands represent the  $g'_{NN}$  and  $g'_{N\Delta}$  dependences with  $g'_{NN} = 0.65 \pm 0.15$  and  $g'_{N\Delta} = 0.35 \pm 0.15$ . In the continuum RPA, the GT state couples to particle-unbound  $1^+$  states, which shifts the response function in coordinate space to larger  $r$  values. Thus the angular distributions further shift to lower momentum transfer. Furthermore, the RPA correlation enhances all three  $ID_i$  at large momentum transfers of  $q \simeq 1.6 \text{ fm}^{-1}$ , improving the agreement with the data. In the analysis of QES, the spin-transverse  $ID_p$  and  $ID_n$  are quenched due to the repulsion of the spin-transverse interaction  $V_T$  [23, 25]. However, in the analysis shown in Fig. 12, the transition form factors are normalized to reproduce  $B(\text{GT})$ . This means that the quenching due to the repulsive LM interaction is effectively included through the normalization factor  $N$  [32]. Therefore, in Fig. 12, the attractive rho-meson exchange effects are seen as an enhancement of  $ID_p$  and  $ID_n$  at  $q \simeq 1.6 \text{ fm}^{-1}$ . Also note that the modification of the momentum transfer dependences (due to the shape change of the response functions in  $r$ -space which is not included through the normalization) is important for the magnitude of  $ID_i$ .

In some theoretical studies [10, 66, 67], the LM parameters are taken to have the

momentum- and energy-transfer dependence. We investigated this effect on  $ID_i$  by using the effective interaction  $V_{\text{eff}}$  by Alberico *et al.* [10], in which the LM parameters have the momentum- and energy-transfer dependence with the dipole form factors. The DWIA+RPA results with this effective interaction are shown in Fig. 13. The dashed and solid curves correspond to the calculations with and without the dipole form factors, respectively. We note that the coupling constants and meson parameters are slightly different from those in Ref. [59], and thus the results without the dipole form factors are also slightly different from those shown in Fig. 12. For the spin-longitudinal mode, the use of the dipole form factors enhances  $ID_q$  at large momentum transfers of  $q \simeq 1.6 \text{ fm}^{-1}$ , which is due to the more attractive spin-longitudinal interaction  $V_L$ . However, the effect is small, and the same results can be achieved by using smaller and reasonable LM parameters of  $g'_{NN} \simeq 0.55$  and  $g'_{N\Delta} \simeq 0.30$ . For the spin-transverse mode, the form factor effects are very small in both  $ID_p$  and  $ID_n$  because of the insensitivity to the spin-transverse interaction  $V_T$  [1].

Figure 14 compares the experimental and theoretical results for the cross section and orthogonal components of the polarization transfer observables,  $D_{NN}$ ,  $D_{S'S}$ , and  $D_{L'L}$ . These quantities are better reproduced by considering RPA correlations together with the nonlocality of the nuclear mean field, particularly for the momentum transfer dependences. From the analyses in Figs. 12 and 14, we conclude that our data support the existence of pionic and rho-mesonic correlations in nuclei at large momentum transfers.

## VI. FINAL REMARKS

The DWIA calculations including RPA correlations reproduce the experimental data for the spin-longitudinal cross section  $ID_q$  and give improved descriptions of the spin-transverse cross sections,  $ID_p$  and  $ID_n$ . However, the experimental values of  $ID_p$  and  $ID_n$  remain larger than the calculated values at momentum transfers of  $q \simeq 1.6 \text{ fm}^{-1}$  by factors of about 1.4 and 2.0, respectively. The magnitudes of the observed enhancements are significantly different for  $ID_p$  and  $ID_n$ . Since the spin-transverse response is common for  $ID_p$  and  $ID_n$ , medium modifications of the effective  $NN$  interaction are considered as a possible reason for the observed enhancements. Such modifications have been discussed using data for the stretched state excitations in Refs. [31, 68, 69], where it is reported that the experimental values of  $ID_n$  at large momentum transfers are increased in magnitude by a factor of about

1.5, indicating an enhancement in the corresponding  $NN$  scattering amplitude  $B$ . Thus, a larger value of  $B$  might be responsible for the enhancement in the experimental values of  $ID_n$  from Eq. (8). However, since no modification of the  $NN$  amplitude  $F$  is observed in the stretched state excitations, the enhancement in  $ID_p$  cannot be explained by modifications of the  $NN$  interaction. We note that medium modifications of the effective  $NN$  interaction have been also discussed in the relativistic framework [70]. If one takes into account the increase in  $B$ , the enhancement of  $ID_n$  is reduced to 1.3, which is almost same as that of  $ID_p$ . Consequently the experimental values of  $ID_p$  and  $ID_n$  may be enhanced by a common mechanism, such as higher order (e.g., 2p-2h) configuration mixing [71, 72]. Thus more comprehensive and detailed theoretical analyses are needed including effects of higher order configuration mixing and medium modifications of the effective  $NN$  interaction.

## VII. SUMMARY AND CONCLUSION

We have measured differential cross sections and complete sets of polarization observables for the  $^{12}\text{C}(\vec{p}, \vec{n})^{12}\text{N}(\text{g.s.}, 1^+)$  reaction at  $T_p = 296$  MeV with momentum transfers of  $q = 0.1$  to  $2.2 \text{ fm}^{-1}$  in order to investigate nuclear correlation effects inside the nuclei. The experimental polarized cross sections  $ID_i$  have been compared with DWIA calculations employing shell-model wave functions. For all three spin-dependent  $ID_i$ , a significant difference in the momentum-transfer dependence and an enhancement around  $q \simeq 1.6 \text{ fm}^{-1}$  were observed when compared to calculations. The use of a local effective mass of  $m^*(0) = 0.7m_N$  improves the agreement with the data, but still underestimates the cross section at around  $q \simeq 1.6 \text{ fm}^{-1}$ . These underestimations for all three spin-dependent  $ID_i$  are partly resolved by DWIA calculations employing an RPA response function with  $g'_{NN} = 0.65$ ,  $g'_{N\Delta} = 0.35$ , and  $m^*(0) = 0.7m_N$ , supporting the existence of pionic and rho-mesonic correlations in the nuclei. This finding is the first indication for observing pionic and rho-mesonic correlation effects separately. To understand the nuclear correlation effects quantitatively, theoretical analyses are required that include effects of higher order configuration mixing and medium modifications in the effective  $NN$  interaction.

## **Acknowledgments**

We thank the RCNP cyclotron crew for providing a good quality beam for this experiment, performed under Program Number E256. This work was supported by Grants-in-Aid for Scientific Research Nos. 14702005 and 16654064 from the Ministry of Education, Culture, Sports, Science, and Technology of Japan.

- 
- [1] M. Ichimura, H. Sakai, and T. Wakasa, *Prog. Part. Nucl. Phys.* **56**, 446 (2006).
- [2] T. Wakasa et al., *Phys. Rev. C* **55**, 2909 (1997).
- [3] K. Yako et al., *Phys. Lett.* **B615**, 193 (2005).
- [4] A. B. Migdal, *Zh. Eksp. Teor. Fiz.* **61**, 2210 (1971); *Sov. Phys. JETP* **34**, 1184 (1972).
- [5] P. O. Slane, D. J. Helfand, and S. S. Murray, *Astrophys. J.* **571**, L45 (2002).
- [6] S. Tsuruta, M. A. Teter, T. Takatsuka, T. Tatsumi, and R. Tamagaki, *Astrophys. J.* **571**, L143 (2002).
- [7] H. Toki and W. Weise, *Phys. Rev. Lett.* **42**, 1034 (1979).
- [8] J. Delorme, M. Ericson, A. Figureau, and N. Giraud, *Phys. Lett.* **B89**, 327 (1980).
- [9] W. M. Alberico, M. Ericson, and A. Molinari, *Phys. Lett.* **B92**, 153 (1980).
- [10] W. M. Alberico, M. Ericson, and A. Molinari, *Nucl. Phys.* **A379**, 429 (1982).
- [11] J. R. Comfort and W. G. Love, *Phys. Rev. Lett.* **44**, 1656 (1980).
- [12] J. R. Comfort, S. M. Austin, P. T. Debevec, G. L. Moake, R. W. Finlay, and W. G. Love, *Phys. Rev. C* **21**, 2147 (1980).
- [13] M. Haji-Saeid et al., *Phys. Rev. Lett.* **45**, 880 (1980).
- [14] J. R. Comfort, R. E. Segel, G. L. Moake, D. W. Miller, and W. G. Love, *Phys. Rev. C* **23**, 1858 (1981).
- [15] T. A. Carey, K. W. Jones, J. B. McClelland, J. M. Moss, L. B. Rees, N. Tanaka, and A. D. Bacher, *Phys. Rev. Lett.* **53**, 144 (1984).
- [16] L. B. Rees, J. M. Moss, T. A. Carey, K. W. Jones, J. B. McClelland, N. Tanaka, A. D. Bacher, and H. Esbensen, *Phys. Rev. C* **34**, 627 (1986).
- [17] R. Fergerson, J. McGill, C. Glashauser, K. Jones, S. Nanda, S. Zuxun, M. Barlett, G. Hoffmann, J. Marshall, and J. McClelland, *Phys. Rev. C* **38**, 2193 (1988).
- [18] O. Häusser et al., *Phys. Rev. Lett.* **61**, 822 (1988).
- [19] C. Chan et al., *Nucl. Phys.* **A510**, 713 (1990).
- [20] J. B. McClelland et al., *Phys. Rev. Lett.* **69**, 582 (1992).
- [21] X. Y. Chen et al., *Phys. Rev. C* **47**, 2159 (1993).
- [22] T. N. Taddeucci et al., *Phys. Rev. Lett.* **73**, 3516 (1994).
- [23] T. Wakasa et al., *Phys. Rev. C* **59**, 3177 (1999).

- [24] C. Hautala et al., Phys. Rev. C **65**, 034612 (2002).
- [25] T. Wakasa et al., Phys. Rev. C **69**, 054609 (2004).
- [26] T. Wakasa et al., Phys. Lett. **B632**, 485 (2006).
- [27] M. A. Franey and W. G. Love, Phys. Rev. C **31**, 488 (1985).
- [28] H. Sakai, H. Okamura, H. Otsu, T. Wakasa, S. Ishida, N. Sakamoto, T. Uesaka, Y. Satou, S. Fujita, and K. Hatanaka, Nucl. Instrum. Methods Phys. Res. A **369**, 120 (1996).
- [29] T. Wakasa et al., Nucl. Instrum. Methods Phys. Res. A **547**, 569 (2005).
- [30] T. Wakasa et al., Nucl. Instrum. Methods Phys. Res. A **404**, 355 (1998).
- [31] T. Wakasa et al., Phys. Lett. **B645**, 402 (2007).
- [32] T. Wakasa et al., Phys. Lett. **B656**, 38 (2007).
- [33] M. Dozono et al., J. Phys. Soc. Jpn. **77**, 014201 (2008).
- [34] T. Wakasa et al., Phys. Rev. C **77**, 054611 (2008).
- [35] E. Ihara et al., Phys. Rev. C **78**, 024607 (2008).
- [36] K. Hatanaka, K. Takahisa, H. Tamura, M. Sato, and I. Miura, Nucl. Instrum. Methods Phys. Res. A **384**, 575 (1997).
- [37] M. Kondo et al., in *Proceedings of the 7th International Conference on Cyclotrons and their Applications*, edited by W. Joho (Birkhäuser, Basel, 1975).
- [38] I. Miura et al., in *Proceedings of the 13th International Conference on Cyclotrons and their Applications*, edited by M. K. Craddock (World Scientific, Singapore, 1993).
- [39] T. N. Taddeucci et al., Phys. Rev. C **41**, 2548 (1990).
- [40] T. Wakasa et al., J. Phys. Soc. Japan **73**, 1611 (2004).
- [41] T. Wakasa et al., Phys. Rev. C **51**, R2871 (1995).
- [42] A. Tamii et al., Nucl. Instrum. Methods Phys. Res. A **605**, 326 (2009).
- [43] R. Schaeffer, J. Raynal, Program DW70 (unpublished); J. Raynal, Nucl. Phys. **A97**, 572 (1967); J. R. Comfort, Extended version DW81 (unpublished).
- [44] S. Hama, B. C. Clark, E. D. Cooper, H. S. Sherif, and R. L. Mercer, Phys. Rev. C **41**, 2737 (1990).
- [45] E. D. Cooper, S. Hama, B. C. Clark, and R. L. Mercer, Phys. Rev. C **47**, 297 (1993).
- [46] B. A. Brown et al., The Oxford-Buenos Aires-MSU shell model code OXBASH, Michigan State University Cyclotron Report 524, 1986.
- [47] S. Cohen and D. Kurath, Nucl. Phys. **73**, 1 (1965).

- [48] D. E. Alburger and A. M. Nathan, *Phys. Rev. C* **17**, 280 (1978).
- [49] K. Schreckenbach, P. Liaud, R. Kossakowski, H. Nastoll, A. Bussiere, and J. P. Guillaud, *Phys. Lett.* **B349**, 427 (1995).
- [50] A. Bohr and B. R. Mottelson, *Nuclear structure Volume I : Single-Particle Motion* (Benjamin, New York, 1969).
- [51] K. Nishida and M. Ichimura, *Phys. Rev. C* **51**, 269 (1995).
- [52] E. Bleszynski, M. Bleszynski, and J. C. A. Whitten, *Phys. Rev. C* **26**, 2063 (1982).
- [53] M. Ichimura and K. Kawahigashi, *Phys. Rev. C* **45**, 1822 (1992).
- [54] F. T. Baker et al., *Phys. Rev. C* **48**, 1106 (1993).
- [55] S. Qing-biao, F. Da-chun, and Z. Yi-zhong, *Phys. Rev. C* **43**, 2773 (1991).
- [56] B. L. Clausen, R. J. Peterson, and R. A. Lindgren, *Phys. Rev. C* **38**, 589 (1988).
- [57] J. R. Comfort, G. L. Moake, C. C. Foster, P. Schwandt, C. D. Goodman, J. Rapaport, and W. G. Love, *Phys. Rev. C* **24**, 1834 (1981).
- [58] K. Kawahigashi, K. Nishida, A. Itabashi, and M. Ichimura, *Phys. Rev. C* **63**, 044609 (2001).
- [59] R. Machleidt, K. Holinde, and C. Elster, *Phys. Rep.* **149**, 1 (1987).
- [60] T. Wakasa, M. Ichimura, and H. Sakai, *Phys. Rev. C* **72**, 067303 (2005).
- [61] W. H. Dickhoff, A. Faessler, J. M. ter Vehn, and H. Mütter, *Phys. Rev. C* **23**, 1154 (1981).
- [62] N. V. Giai and P. V. Thieu, *Phys. Lett.* **B126**, 421 (1983).
- [63] C. Mahaux and R. Sartor, *Nucl. Phys.* **A481**, 381 (1988).
- [64] W. G. Love and M. A. Franey, *Phys. Rev. C* **24**, 1073 (1981).
- [65] F. G. Perey and B. Buck, *Nucl. Phys.* **32**, 353 (1962).
- [66] H. Oset, H. Toki, and W. Weise, *Phys. Rep.* **83**, 281 (1982).
- [67] J. Speth, V. Klemt, J. Wambach, and G. E. Brown, *Nucl. Phys.* **A343**, 382 (1980).
- [68] E. J. Stephenson, J. Liu, A. D. Bacher, S. M. Bowyer, S. Chang, C. Olmer, S. P. Wells, S. W. Wissink, and J. Lisantti, *Phys. Rev. Lett.* **78**, 1636 (1997).
- [69] K. Yako et al., in *Proceedings of the RCNP International Symposium in Nuclear Responses and Medium Effects*, edited by T. Noro, H. Sakaguchi, H. Sakai, and T. Wakasa (Universal Academy Press, Tokyo, 1998).
- [70] G. C. Hillhouse, B. I. S. van der Ventel, S. M. Wyngaardt, and P. R. D. Kock, *Phys. Rev. C* **57**, 448 (1998).
- [71] W. M. Alberico, M. Ericson, and A. Molinari, *Ann. Phys. (N.Y.)* **154**, 356 (1984).

[72] J. P. Adams and B. Castel, Phys. Rev. C **50**, R1763 (1994).



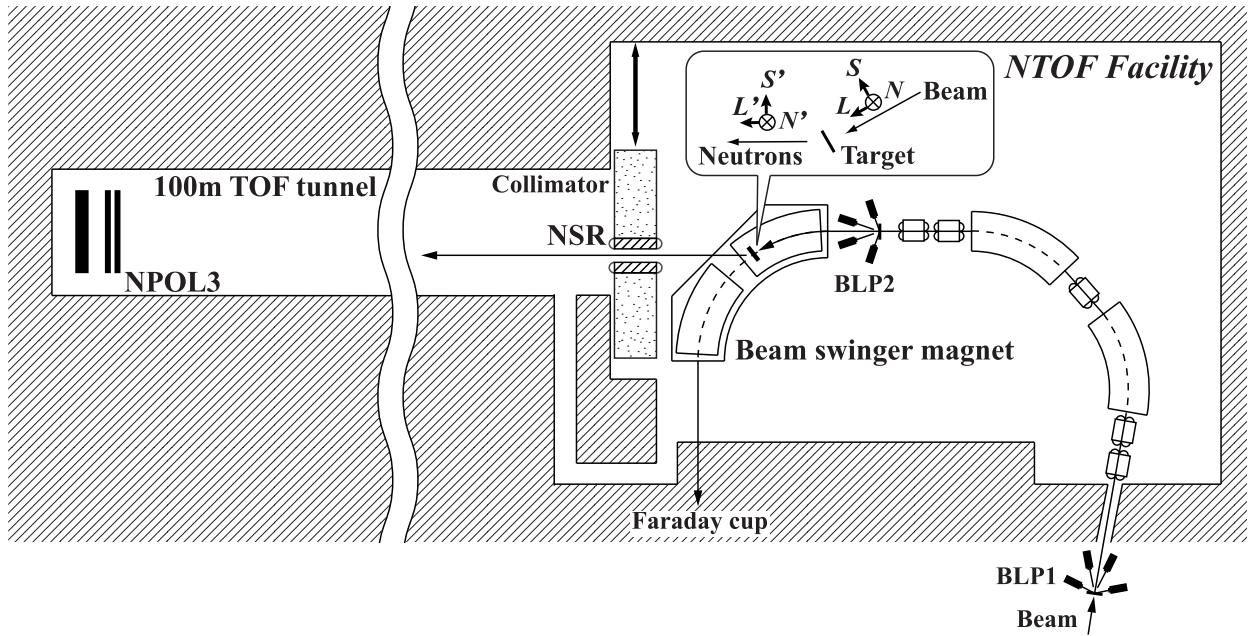


FIG. 1: A schematic layout of the NTOF facility (not to scale). The coordinate systems for incident protons and outgoing neutrons are also shown.  $S$  (Sideways),  $N$  (Normal) and  $L$  (Longitudinal) form a right-handed system for incident protons and  $S'$ ,  $N'$ ,  $L'$  for outgoing neutrons.

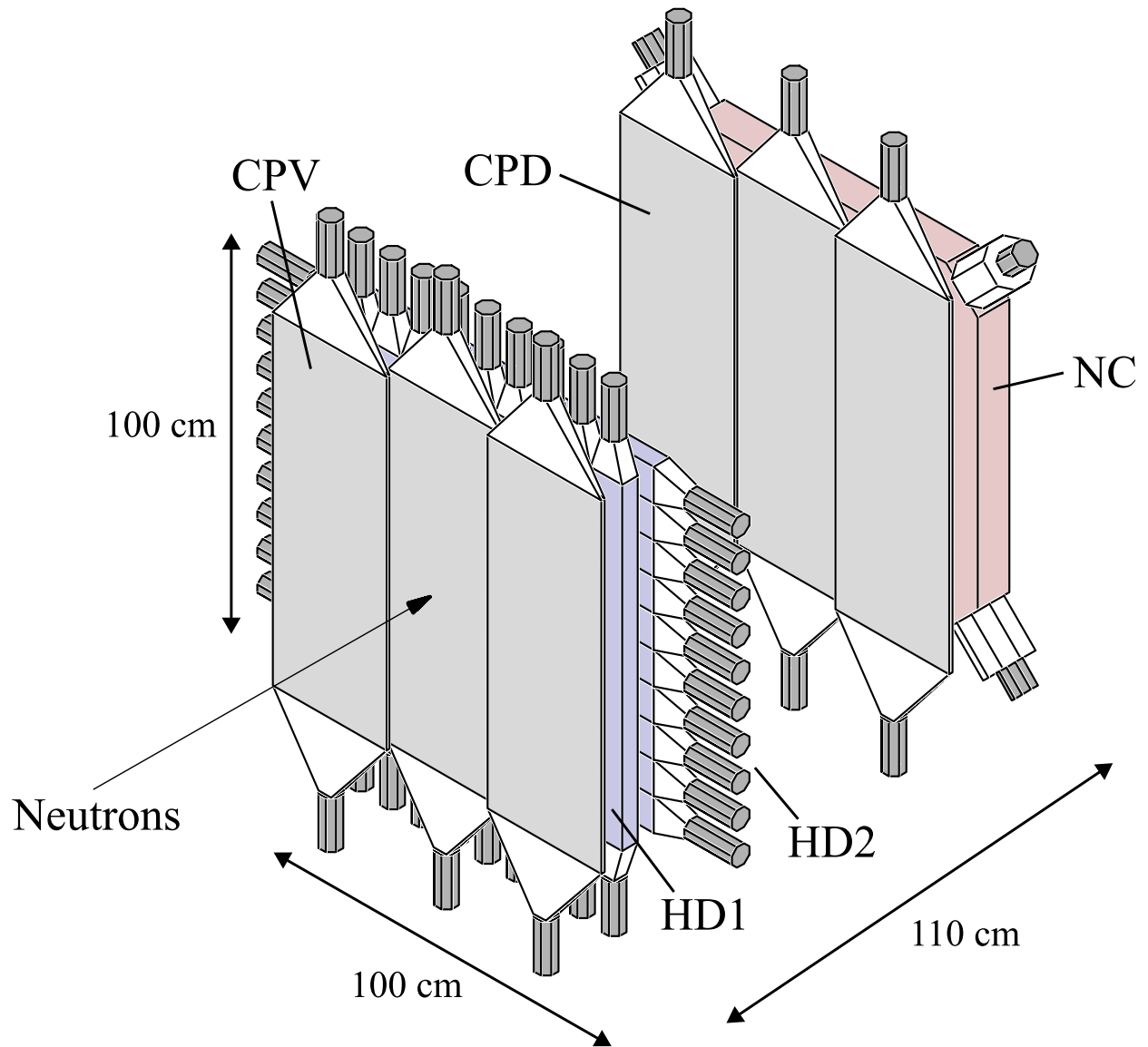


FIG. 2: (Color online) A schematic view of the neutron detector/polarimeter NPOL3. In the detector mode, HD1 and HD2 act as neutron detectors. In the polarimetry mode, HD1 and HD2 are the analyzer planes while NC is the catcher plane. Thin plastic scintillator planes are used to veto (CPV) or identify (CPD) charged particles.

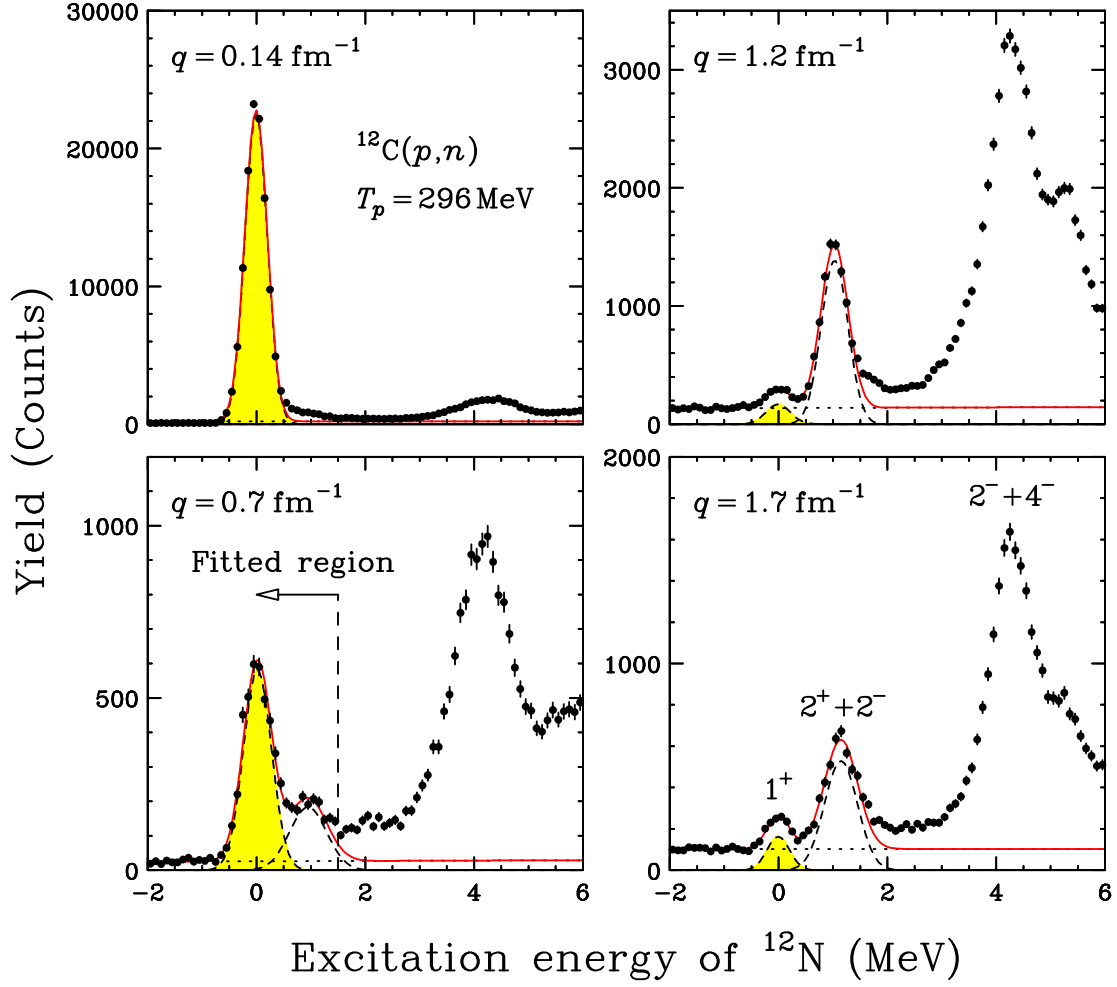


FIG. 3: (Color online) Excitation energy spectra for  $^{12}\text{C}(p,n)^{12}\text{N}$  at  $T_p = 296 \text{ MeV}$  and  $q = 0.14, 0.7, 1.2,$  and  $1.7 \text{ fm}^{-1}$ . The dashed curves are fits to the individual peaks. The solid curves indicate the sum of the peak contributions including the background plotted as the straight dotted lines.

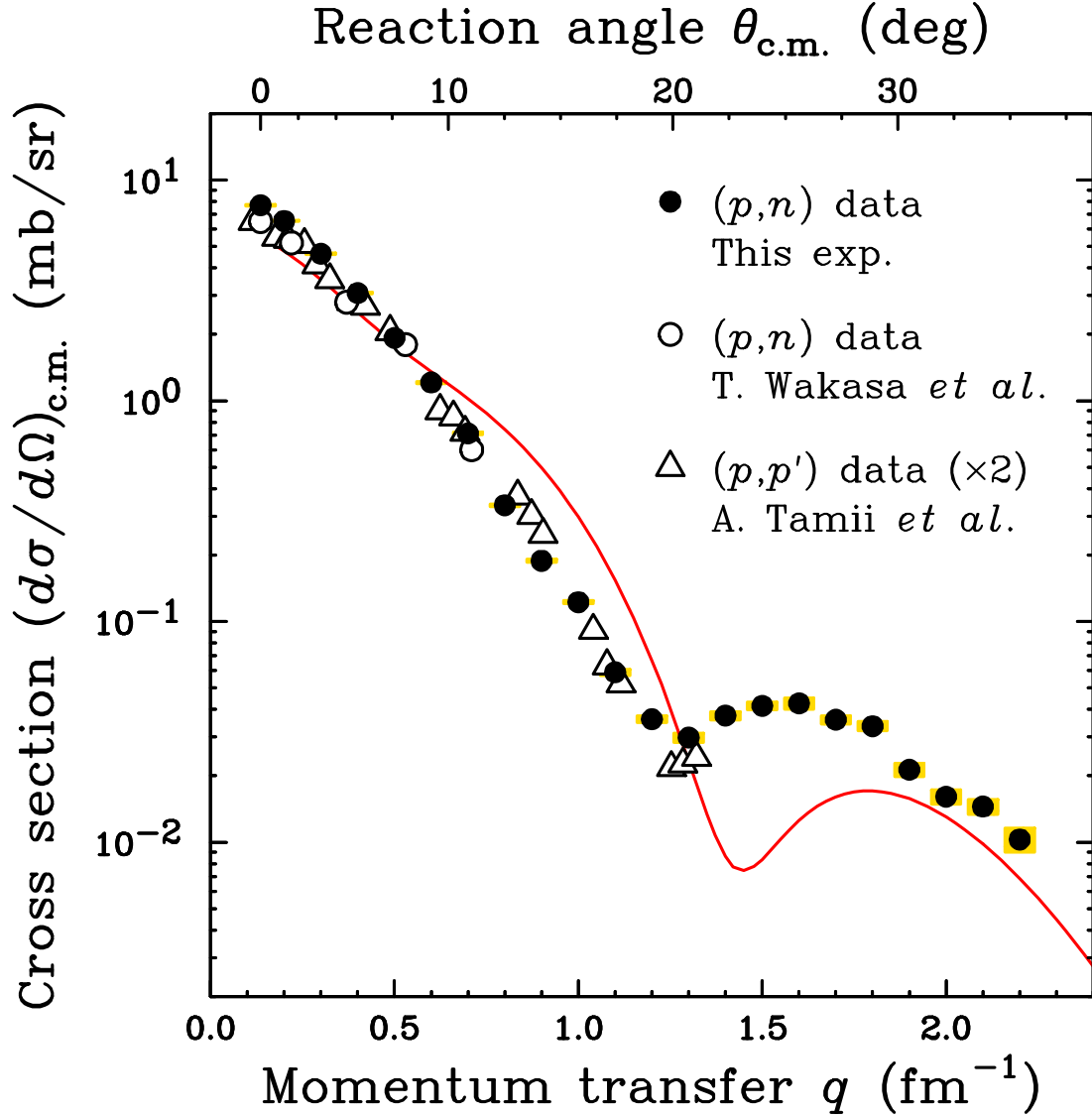


FIG. 4: (Color online) Measured cross sections for  $^{12}\text{C}(p,n)^{12}\text{N}(g.s., 1^+)$  at  $T_p = 296$  MeV (filled circles) as a function of momentum transfer. The corresponding reaction angle  $\theta_{c.m.}$  is also shown on the top of the figure. The open circles are data at  $T_p = 295$  MeV [41]. The open triangles are  $^{12}\text{C}(p,p')^{12}\text{C}^*(1^+, T = 1)$  data at  $T_p = 295$  MeV [42], multiplied by a factor of two as described in the text. The solid curve shows DWIA calculations using a shell-model wave function.

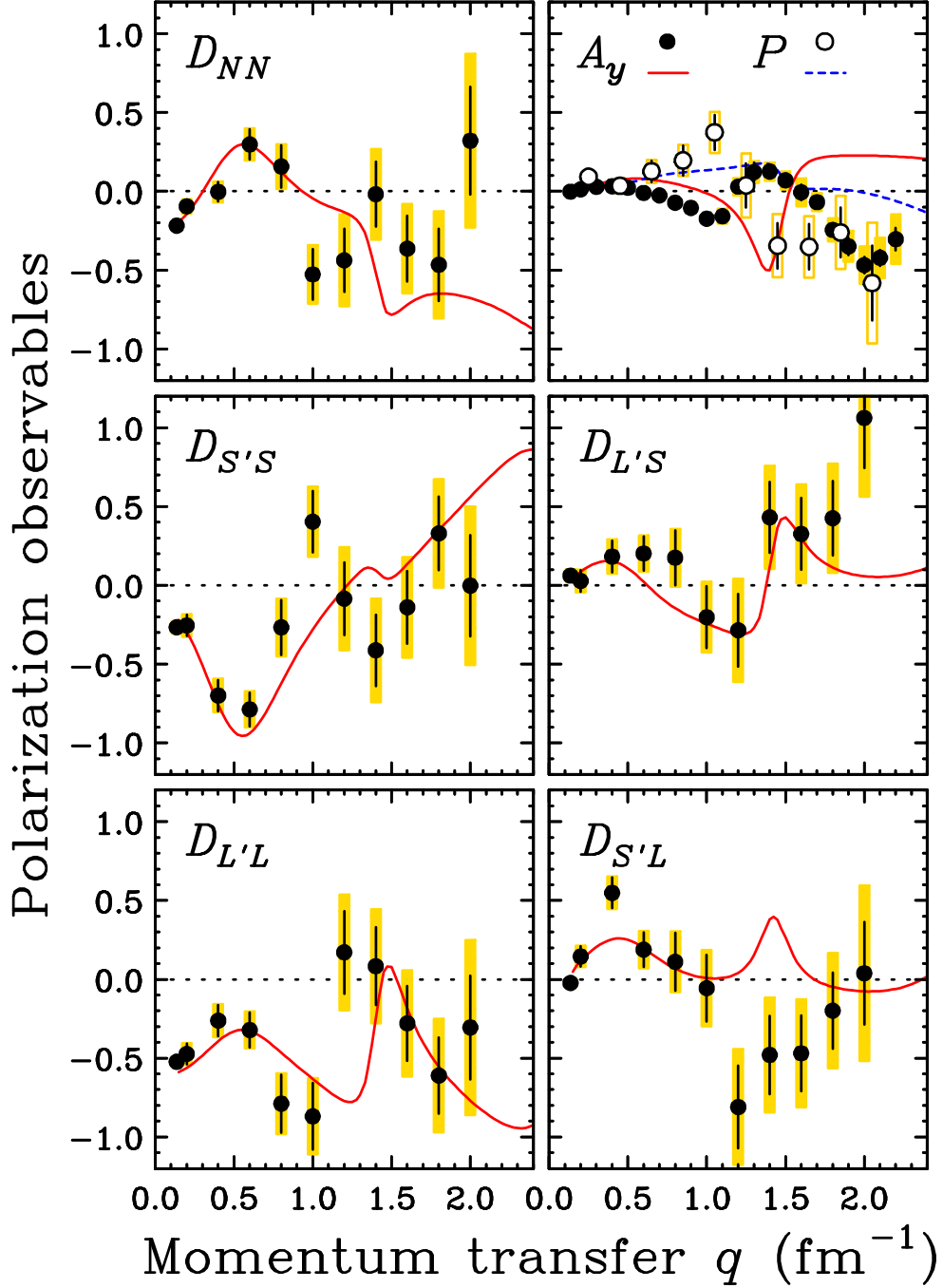


FIG. 5: (Color online) Measured polarization transfer observables  $D_{ij}$ , analyzing power  $A_y$ , and induced polarization  $P$  for  $^{12}\text{C}(p, n)^{12}\text{N}(\text{g.s.}, 1^+)$  at  $T_p = 296$  MeV. The induced polarization data  $P$  are offset by a momentum transfer of  $0.05 \text{ fm}^{-1}$  so that the analyzing power  $A_y$  and induced polarization  $P$  data can be distinguished. The solid and dashed curves are the results of DWIA calculations with a shell-model wave function.

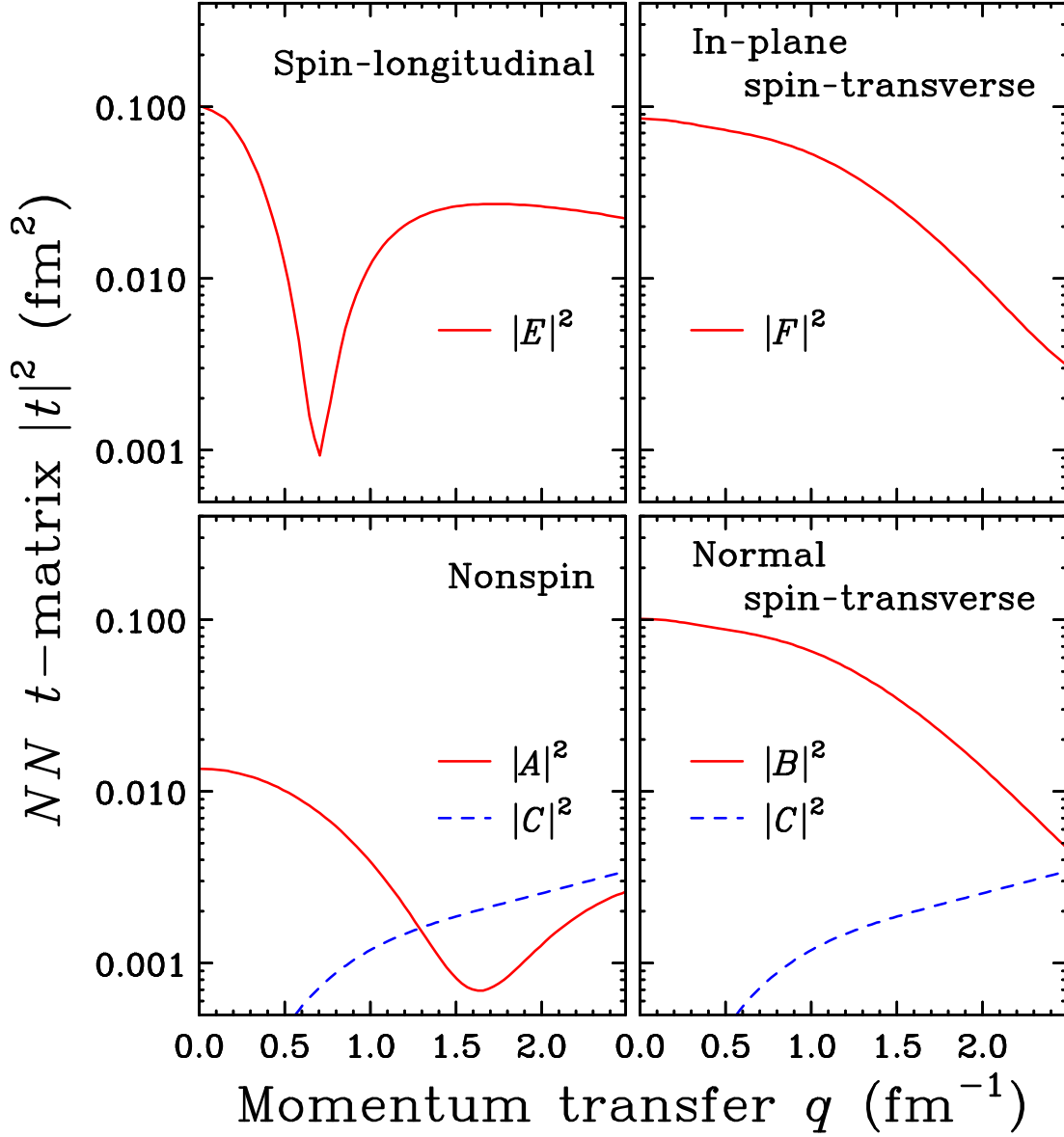


FIG. 6: (Color online) Squared  $t$ -matrix components calculated from the FL  $t$ -matrix at 325 MeV.

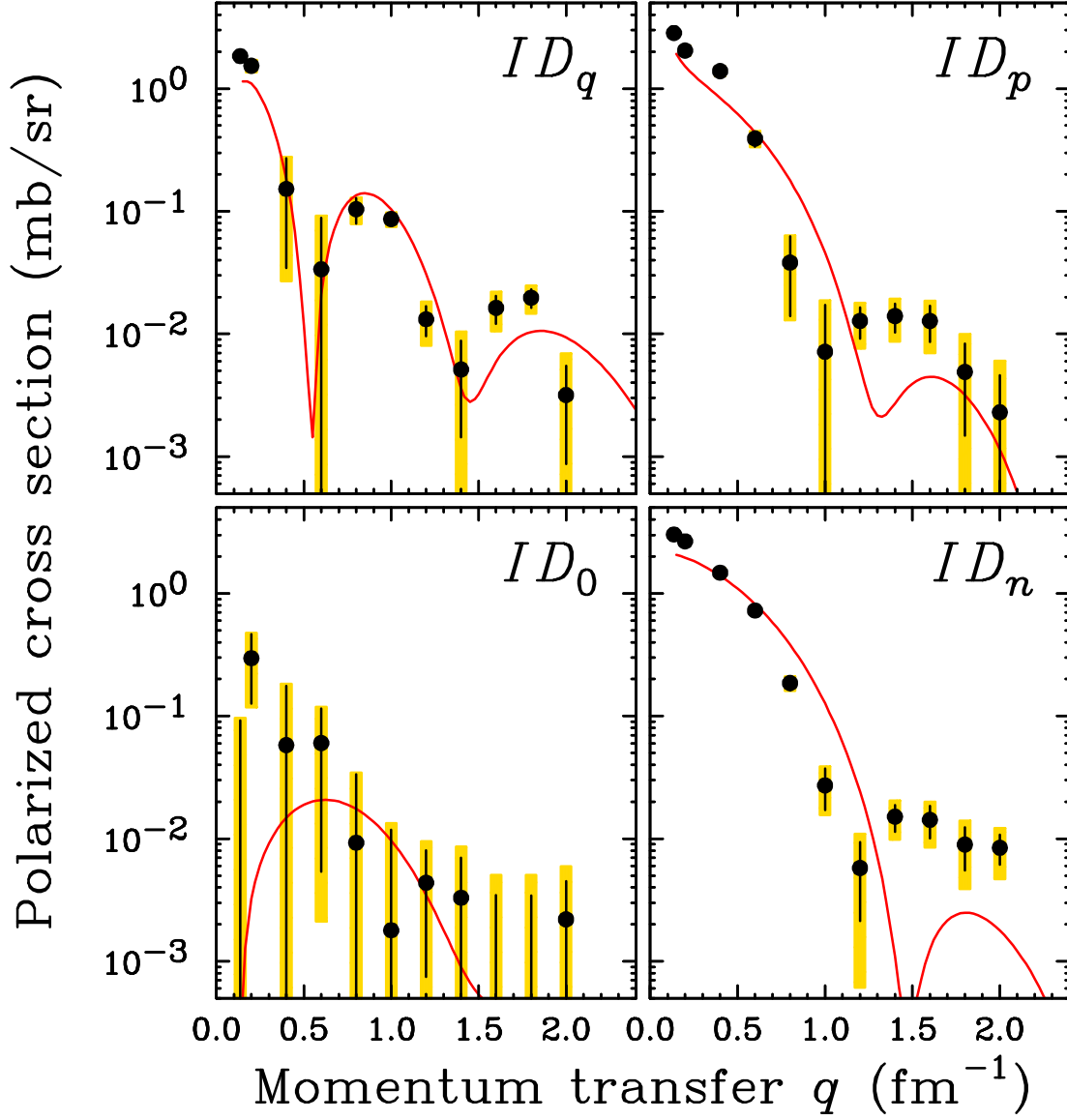


FIG. 7: (Color online) Measured polarized cross sections for  $^{12}\text{C}(p,n)^{12}\text{N}(\text{g.s.}, 1^+)$  at  $T_p = 296$  MeV. The solid curves are the results of DWIA calculations using the shell-model wave function.

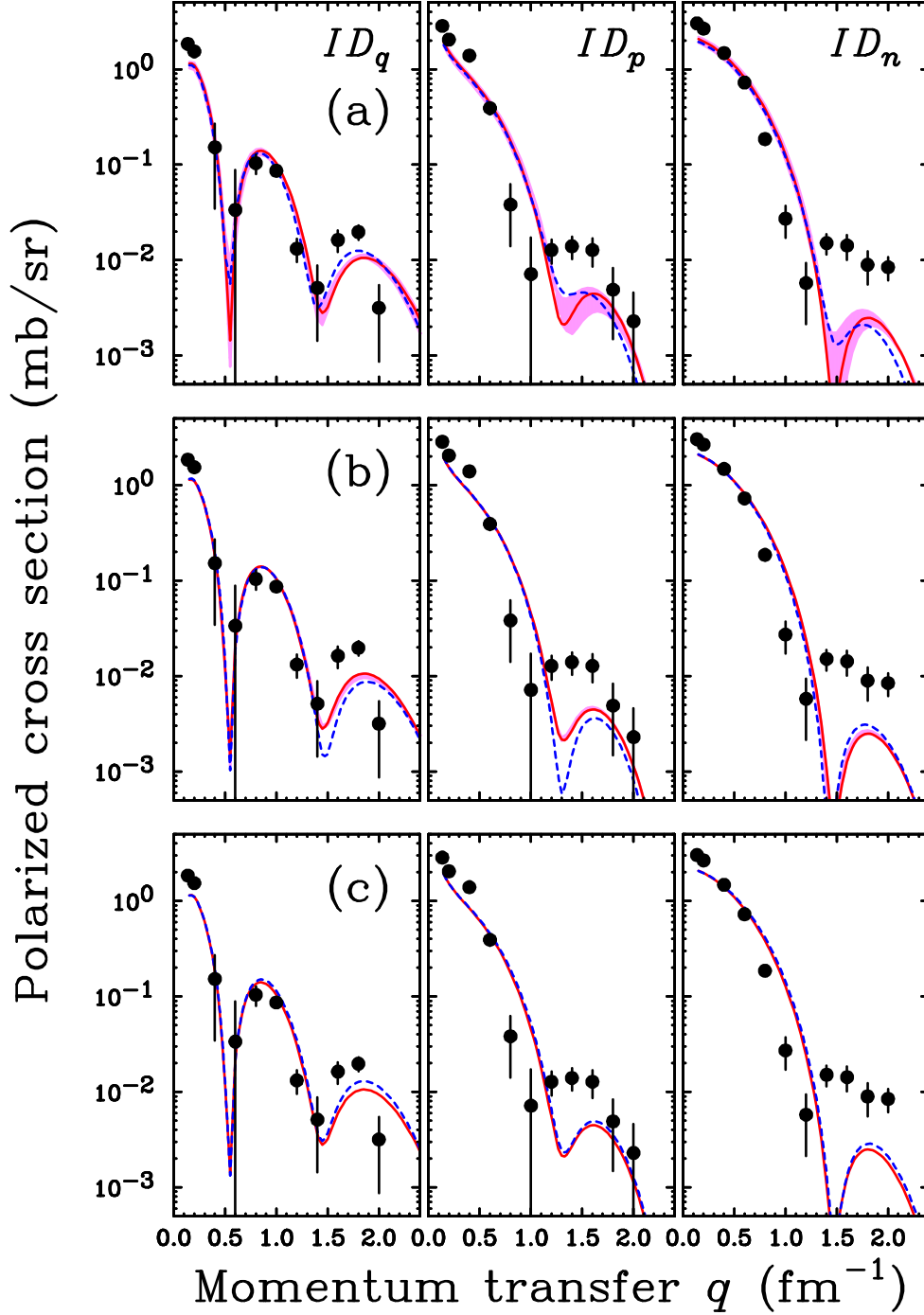


FIG. 8: (Color online) Parameter dependence of the calculations for the spin-dependent polarized cross sections  $ID_q$  (left panels),  $ID_p$  (middle panels), and  $ID_n$  (right panels). The solid curves are the same as those in Fig. 7. The bands and dashed curves present DWIA results with other parameters: (a) four different OMP parameters (bands) and neutron global OMPs for the exit channel (dashed curves); (b) two different CKWFs (bands) and a pure  $0p_{1/2}0p_{3/2}^{-1}$  configuration (dashed curves); and (c) the HO potential (dashed curves).



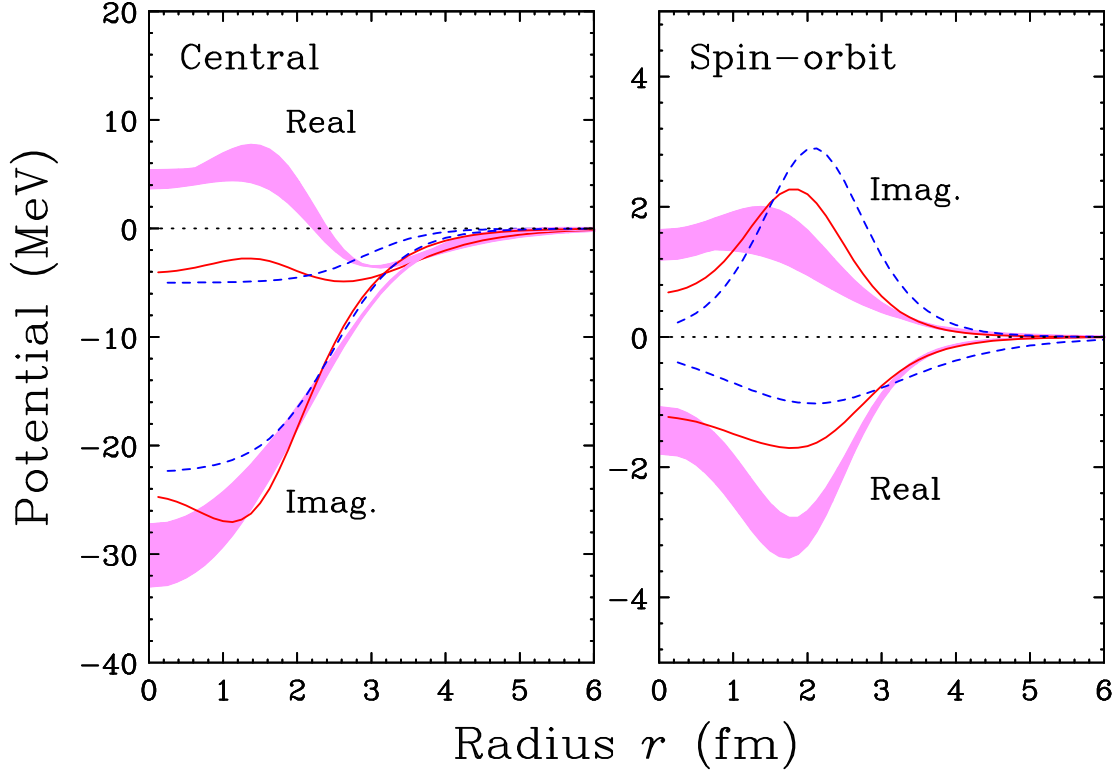


FIG. 9: (Color online) The radial dependences of the OMPs for the incident channel used in the DWIA calculations. The solid curves and the bands show the global OMPs optimized for  $^{12}\text{C}$  (EDAI) and  $^{12}\text{C}-^{208}\text{Pb}$  (EDAI Fit 1-3) in the proton energy range of  $T_p = 20-1040$  MeV, respectively [44, 45]. The dashed curves represent the OMP obtained from proton elastic scattering data on  $^{12}\text{C}$  at  $T_p = 318$  MeV [54].

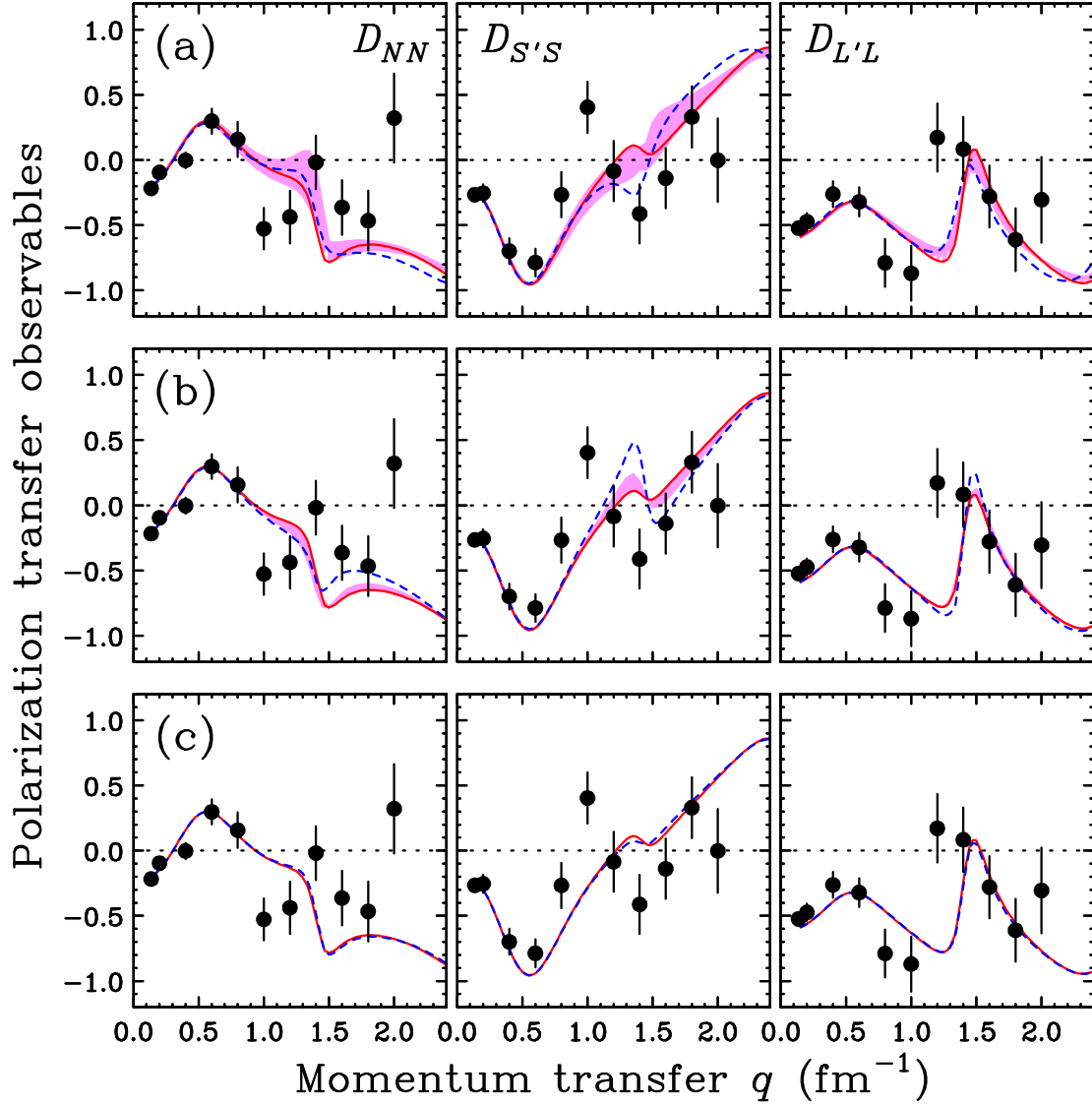


FIG. 10: (Color online) Same as in Fig. 8 but for the diagonal polarization transfer observables:  $D_{NN}$  (left panels),  $D_{S'S}$  (middle panels), and  $D_{L'L}$  (right panels).

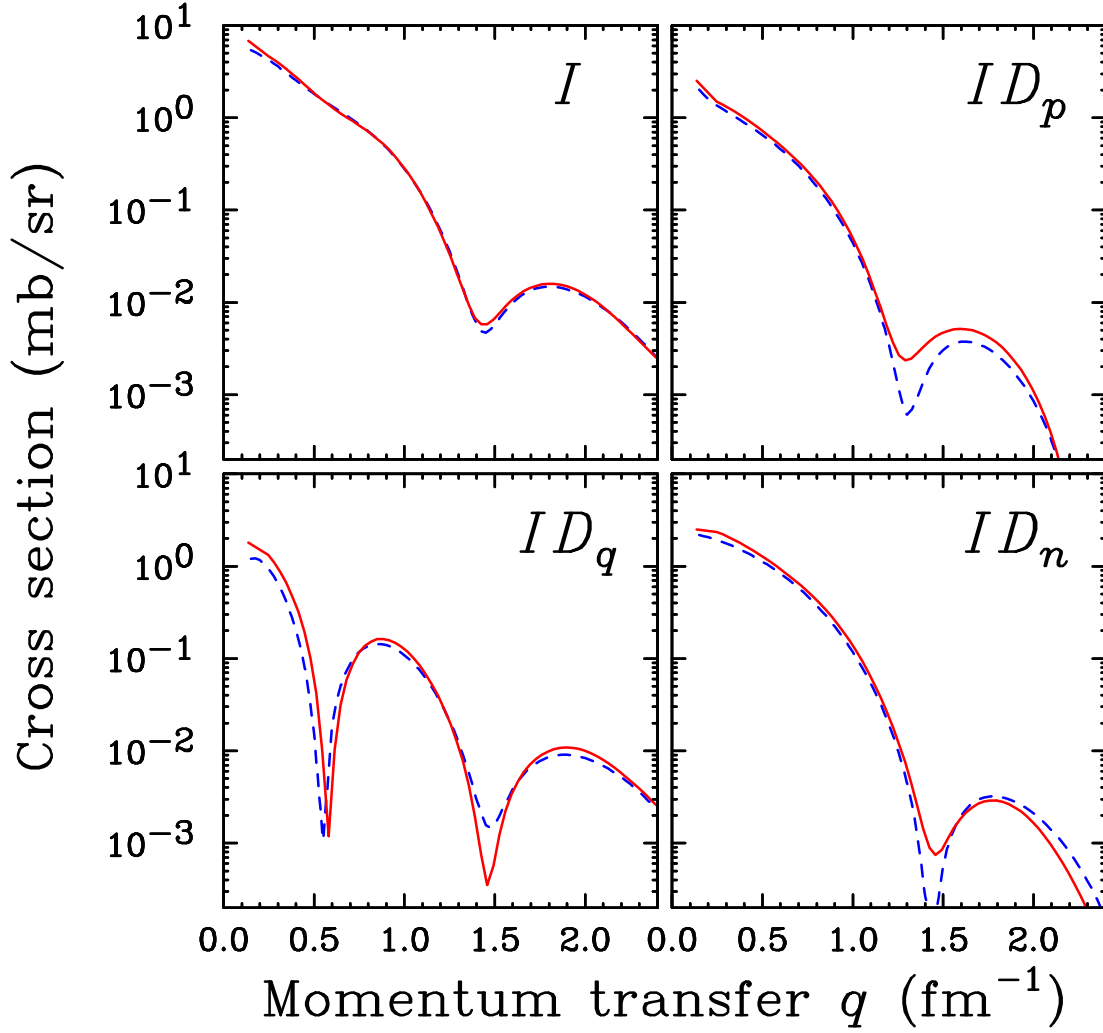


FIG. 11: (Color online) Comparison between calculations using the computer codes CRDW and DW81 for the cross section  $I$  and polarized cross sections,  $ID_q$ ,  $ID_p$ , and  $ID_n$ . The solid and dashed curves represent DWIA calculations using CRDW and DW81, respectively. The normalization factor  $N$  of 0.17 is common for both calculations.

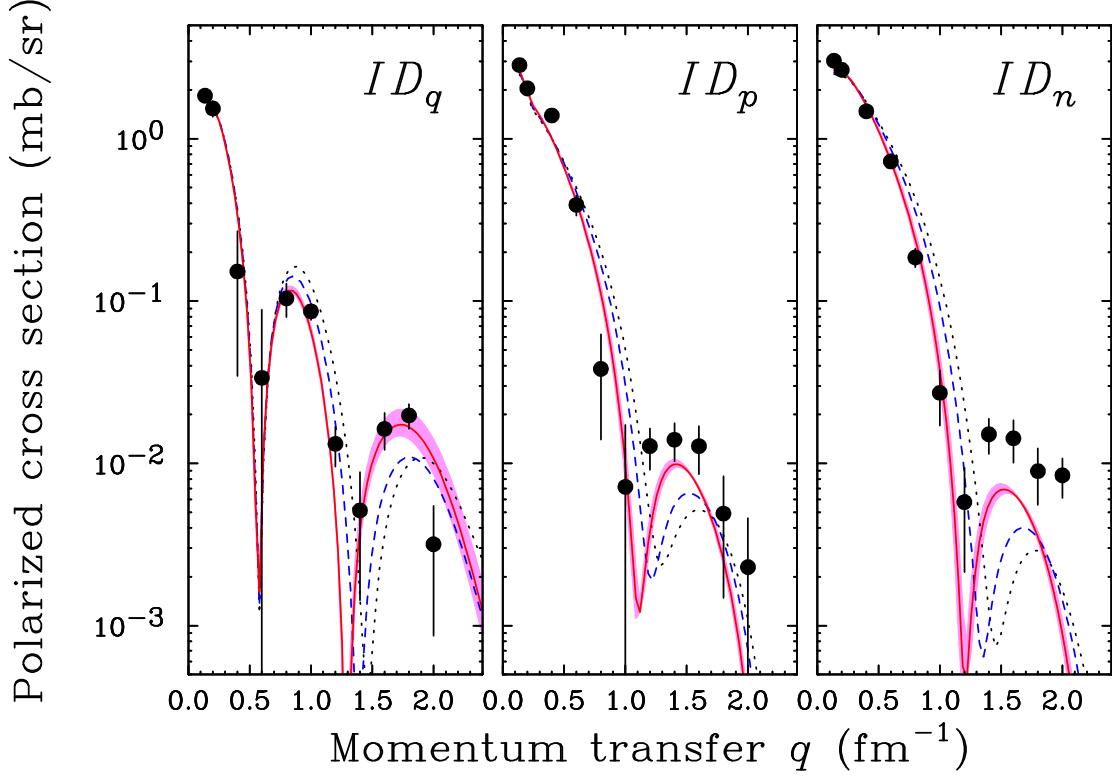


FIG. 12: (Color online) Comparison between experimental and theoretical results of polarized cross sections  $ID_q$ ,  $ID_p$ , and  $ID_n$  for  $^{12}\text{C}(p, n)^{12}\text{N}(\text{g.s.}, 1^+)$  at  $T_p = 296$  MeV. The dotted and dashed curves present the DWIA results with a free response function using  $m^*(0) = m_N$  and  $m^*(0) = 0.7m_N$ , respectively, and  $N = 0.17$ . The solid curves denote DWIA results for an RPA response function with  $(g'_{NN}, g'_{N\Delta}, g'_{\Delta\Delta}) = (0.65, 0.35, 0.50)$ ,  $m^*(0) = 0.7m_N$  and  $N = 0.28$ . The bands are the  $g'_{NN}$  and  $g'_{N\Delta}$  dependences of the DWIA results with  $g'_{NN} = 0.65 \pm 0.15$  and  $g'_{N\Delta} = 0.35 \pm 0.15$ .

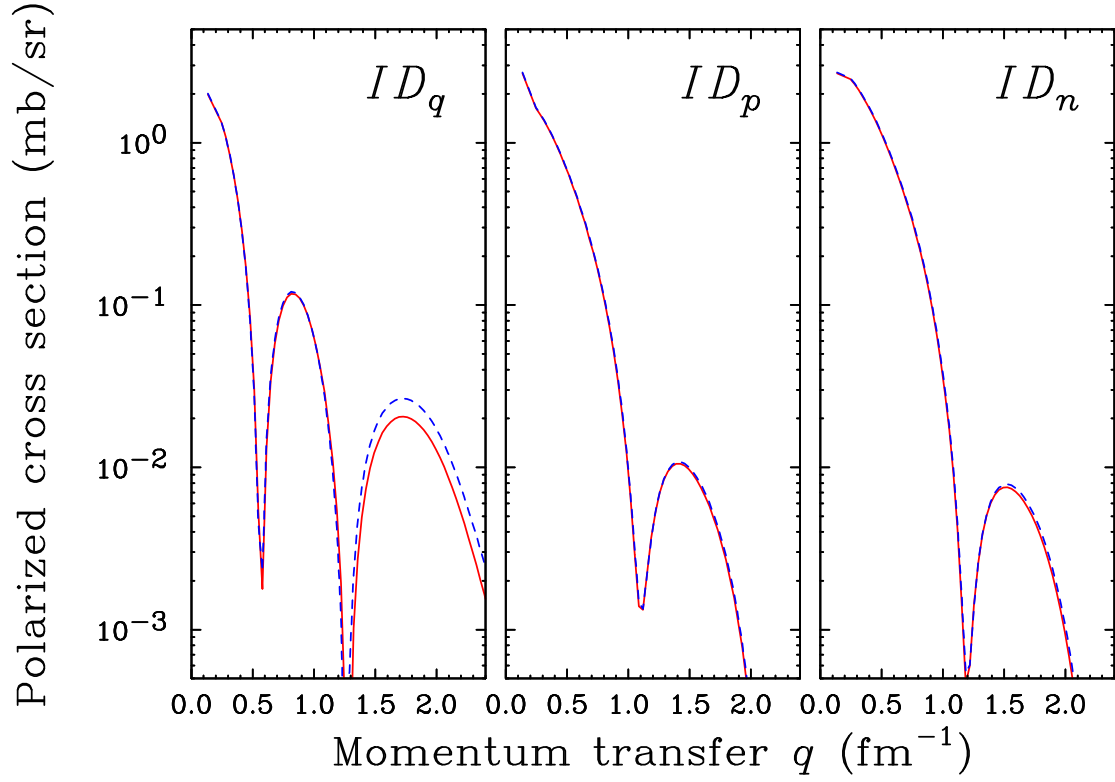


FIG. 13: (Color online) DWIA predictions for  $^{12}\text{C}(p, n)^{12}\text{N}(\text{g.s.}, 1^+)$  at  $T_p = 296$  MeV. The dashed and solid curves are the DWIA results with the RPA response functions using the LM parameters with and without the dipole form factors, respectively.

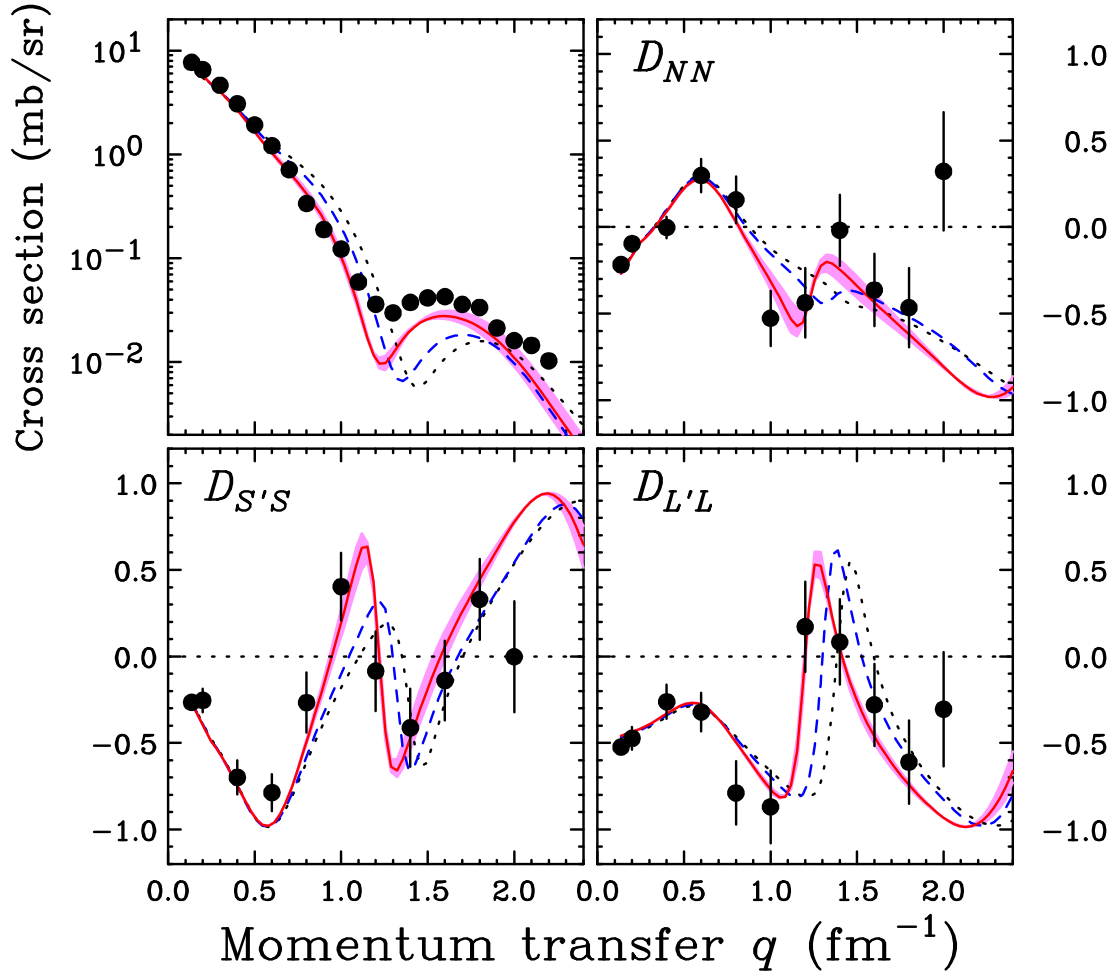


FIG. 14: (Color online) Same as in Fig. 12 but for the cross section and diagonal polarization transfer observables,  $D_{NN}$ ,  $D_{S'S}$ , and  $D_{L'L}$ .